Complete submission Click here to view linked References

STAG2 promotes the myelination transcriptional program in oligodendrocytes

Ningyan Cheng[1], Mohammed Kanchwala[2], Bret M. Evers[3], Chao Xing[2,4], Hongtao Yu[1,5,6,7,*]

[1]Department of Pharmacology, University of Texas Southwestern Medical Center, Dallas, TX 75390, USA.

[2]Eugene McDermott Center for Human Growth and Development, University of Texas Southwestern Medical Center, Dallas, TX 75390, USA.

[3]Division of Neuropathology, University of Texas Southwestern Medical Center, Dallas, TX, 75390, USA.

[4]Department of Bioinformatics, Department of Population and Data Sciences, University of Texas Southwestern Medical Center, Dallas, TX 75390, USA.

[5]Westlake Laboratory of Life Sciences and Biomedicine, Hangzhou, China.

[6]School of Life Sciences, Westlake University, Hangzhou, China.

[7]Institute of Biology, Westlake Institute for Advanced Study, Hangzhou, China.

[*]Correspondence: yuhongtao@westlake.edu.cn

SUMMARY

Cohesin folds chromosomes via DNA loop extrusion. Cohesin-mediated chromosome loops regulate transcription by shaping long-range enhancer-promoter interactions, among other mechanisms. Mutations of cohesin subunits and regulators cause human developmental diseases termed cohesinopathy. Vertebrate cohesin consists of SMC1, SMC3, RAD21, and either STAG1 or STAG2. To probe the physiological functions of cohesin, we created conditional knockout (cKO) mice with *Stag2* deleted in the nervous system. *Stag2* cKO mice exhibit growth retardation, neurological defects, and premature death, in part due to insufficient myelination of nerve fibers. *Stag2* cKO oligodendrocytes exhibit delayed maturation and downregulation of myelination-related genes. *Stag2* loss reduces promoter-anchored loops at downregulated genes in oligodendrocytes. Thus, STAG2-cohesin generates promoter-anchored loops at myelination-promoting genes to facilitate their transcription. Our study implicates defective myelination as a contributing factor to cohesinopathy and establishes oligodendrocytes as a relevant cell type to explore the mechanisms by which cohesin regulates transcription.

INTRODUCTION

Chromosomes in a single human diploid cell, if linearly stitched together, span a length of more than two meters. They need to be properly folded to be housed in the cell nucleus with a diameter of 10 μm. Chromosome folding occurs in a dynamic, structured way that regulates gene expression, and DNA replication and repair. Initially discovered as the molecular glue that tethers sister chromatids for segregation during mitosis (Haarhuis et al., 2014; Uhlmann, 2016; Yatskevich et al., 2019; Zheng and Yu, 2015), the cohesin complex has later been shown to be critical for structured chromosome folding and gene expression (Haarhuis et al., 2017; Rao et al., 2017; Schwarzer et al., 2017; Wutz et al., 2017).

Cohesin is loaded on chromosomes by the cohesin loader NIPBL. The cohesin–NIPBL complex can extrude DNA loops bi-directionally in an ATP-dependent manner (Davidson et al., 2019; Kim et al., 2019; Vian et al., 2018). The chromatin insulator CTCF has been proposed to block loop extrusion by cohesin, establishing topologically associated domains (TADs) and marking TAD boundaries. Chromatin interactions within each TAD are favored whereas inter-TAD interactions are disfavored. Thus, chromosome loops and TADs shape long-range cis-element interactions, such as promoter-enhancer interactions, thereby regulating transcription.

The vertebrate cohesin complex contains four core subunits: the SMC1–SMC3 heterodimeric ATPase, the kleisin subunit RAD21 that links the ATPase heads, and the HEAT-repeat protein STAG1 or STAG2. STAG1 and STAG2 bind to RAD21 in a mutually exclusive manner and create docking sites for several regulatory proteins, including CTCF (Hara et al., 2014; Li et al., 2020). STAG1 and STAG2 also interact with DNA and the SMC1–SMC3 hinge domains (Shi et al., 2020). STAG1 and STAG2 play redundant roles in sister-chromatid cohesion in

cultured human cells, as both need to be simultaneously depleted to produce overt cohesion defects (Hara et al., 2014).

Mutations of NIPBL and cohesin subunits, including STAG2, result in human developmental diseases termed cohesinopathies, which affect multiple organs and systems (Remeseiro et al., 2013b; Soardi et al., 2017). In patients with cohesinopathies, mental retardation and neurological abnormalities caused by brain development defects are common (Piche et al., 2019). Dysregulation of gene transcription as a result of reduced cohesin functions has been suggested to underlie these developmental defects (De Koninck and Losada, 2016; Remeseiro et al., 2013a). In addition, several cohesin genes, including *STAG2*, are frequently mutated in a variety of human cancers (Martincorena and Campbell, 2015).

To better understand the physiological roles of cohesin, we deleted *Stag2* specifically in the nervous system in the mouse. The *Stag2* conditional knockout (cKO) mice exhibited deficient myelination. Loss of STAG2 delayed the maturation of oligodendrocytes and reduced chromosome loops in oligodendrocytes and impaired the transcription of myelination-related genes. Our findings establish the requirement for cohesin in proper gene expression in specific cell types and implicate defective myelination as a potential contributing factor to cohesinopathy.

RESULTS

Stag2 ablation in the nervous system causes growth retardation and neurological defects

Stag1 is required for mammalian embryonic development (Remeseiro et al., 2012), indicating that *Stag2* cannot compensate for the loss of *Stag1*. To examine the roles of *Stag2* during development in the mouse, we targeted a critical exon (exon 8) of *Stag2*, which is located on the X chromosome, using CRISPR-Cas9 (Figure S1A). The *Stag2*^{null} embryos showed severe developmental defects and underwent necrosis by E11.5 days (Figure S1B). Thus, *Stag2* is required for mouse embryonic development, consistent with a recent report (De Koninck et al., 2020). *Stag1* and *Stag2* have non-redundant developmental functions.

Because whole-body knockout of *Stag2* caused embryonic lethality, we created a *Stag2* "floxed" mouse line (*Stag2*$^{f/f}$) by homologous recombination with a template that contained two LoxP sites flanking exon 8 (Figure S2A,B). To study the physiological function of STAG2 in adult mice, we crossed the *Stag2*$^{f/f}$ mice with mice bearing the *Ert2-Cre* genomic insertion and generated *Stag2*$^{f/y}$*;Ert2-Cre* progenies. The *Stag2*$^{f/y}$*;Ert2-Cre* adult mice were injected with tamoxifen to induce *Stag2* deletion in the whole body (Figure S2C). Genotyping analysis of blood extracts showed that tamoxifen induced efficient disruption of the *Stag2* gene locus in *Stag2*$^{f/y}$*;Ert2-Cre* mice (Figure S2D,E). These *Stag2*-deficient adult mice did not show early onset of spontaneous tumor formation, indicating that *Stag2* mutation alone in somatic cells of mice is insufficient to induce tumorigenesis. The *Stag2*-deficient mice also did not have other obvious adverse phenotypes (Figure S2F), except that they had slightly lower body weight (Figure S2G,H), probably due to tissue homeostasis alterations recently reported by others (De Koninck et al., 2020).

STAG2 mutations are found in human cohesinopathy patients with mental retardation and neuropsychiatric behaviors (Soardi et al., 2017). To study the function of STAG2 in the nervous system, we generated *Stag2* conditional knockout mice (*Stag2* cKO) by crossing *Stag2*$^{f/f}$ mice with *Nestin-Cre* mice (Giusti et al., 2014) (Figure 1A,B). The progenies were born in the Mendelian ratio, but *Stag2*$^{f/y}$*;Cre* pups presented growth retardation and premature death (Figure 1C-E). More than 50% *Stag2*$^{f/y}$*;Cre* mice died aged about 3 weeks while the rest died at about 4 months. *Stag2*$^{f/y}$ mice did not show differences discernible from WT littermates. Although *Stag2*$^{f/y}$*;Cre* mice did not present microcephaly, they exhibited frequent hydrocephaly that might contribute to their premature death. The *Stag2*$^{f/y}$*;Cre* mice displayed normal drinking and feeding behaviors (Figure 1F,G), but showed reduced plasma IGF-1 levels compared to the control mice (Figure 1H). *Stag2*$^{f/y}$*;Cre* mice showed forepaw and hindlimb clasping (Figure 1I) and limb tremors (Movie 1), which were not seen in *Stag2*$^{f/y}$ mice. These data indicate that *Stag2* deficiency in the nervous system causes growth retardation and neurological defects.

***Stag2* ablation causes hypomyelination**

Hematoxylin and eosin staining of brain sections of *Stag2*$^{f/y}$*;Cre* mice did not reveal overt anatomical defects (Figure S3A). To understand the origins of neurological defects caused by *Stag2* deletion, we analyzed the gene expression changes in *Stag2*$^{f/y}$*;Cre* mouse brains by RNA-sequencing (RNA-seq) (Figure 2A). Compared with the control groups, 105 and 62 genes were significantly downregulated or upregulated by more than two folds, respectively, in the *Stag2*-deficient brains. The decreased expression of top differentially expressed genes (DEGs) was confirmed by reverse transcription quantitative PCR (RT-qPCR) (Figure 2B). Among the 105 downregulated DEGs in the brains of *Stag2* cKO mice, 44 were enriched in myelin (Figure 2C)

(Thakurela et al., 2016). The Ingenuity Pathway Analysis (IPA) pinpoints cholesterol biosynthesis pathways as the most affected canonical pathways (Figure 2D). We further confirmed that the cholesterol biosynthesis precursors were reduced in *Stag2*$^{f/y}$*;Cre* brains (Figure S3B).

Myelin is the membrane sheath that wraps around axons to facilitate rapid nerve conduction and maintain metabolic supply (Williamson and Lyons, 2018). Dynamic myelination in the central nervous system (CNS) is critical for proper neurodevelopment, and defective myelination is associated with autoimmune and neurodegenerative diseases (Mathys et al., 2019; Wolf et al., 2021). As cholesterol biosynthesis is essential for normal myelination (Hubler et al., 2018; Saher et al., 2005), we hypothesized that depletion of STAG2 caused myelination defects in the nervous system.

Indeed, brain sections of *Stag2*$^{f/y}$*;Cre* mice showed greatly reduced luxol fast blue (LFB) staining compared to those of *Stag2*$^{f/y}$ and *Nestin-Cre* heterozygous mice (Figure 3A and S4A). Immunohistochemistry using antibodies against myelin proteins, MBP and PLP1, confirmed that *Stag2* cKO mice had significant defects in myelin fiber formation (Figure 3B-F). In both cerebral cortex and cerebellum, there were fewer and sparser myelin fibers in *Stag2*$^{f/y}$*;Cre* mice, as compared to the *Stag2*$^{f/y}$ controls. Axon myelin ensheathment was further examined using transmission electron microscopy (Figure 3G). *Stag2*$^{f/y}$*;Cre* mice had significantly fewer myelin-wrapped axons at optic nerves. Collectively, these data indicate insufficient myelination in the *Stag2* cKO mice. Myelination predominantly occurs at 3 weeks after birth in the mouse. The timing of premature death of *Stag2* cKO mice is thus consistent with defective myelination as a contributing factor to the lethality.

STAG2 regulates transcription in OLs

We examined *Stag1* and *Stag2* expression patterns in wild-type mouse brains by *in situ* hybridization using isotope-labeled RNA probes (Figure S4B). Both *Stag1* and *Stag2* were expressed at high levels in hippocampus, medial habenula, neocortex, and cerebellum granular layer. Aside from these regions, the *Stag2* transcripts were detected at relatively high levels in subventricular zone, thalamus, fiber tracts, midbrain, and hindbrain regions. *Stag2* is thus ubiquitously expressed in the brain.

Oligodendrocytes (OLs) are responsible for myelination in the CNS. To examine whether the OL lineage was affected by *Stag2* deletion, we performed single-cell RNA sequencing (scRNA-seq) analysis of *Stag2*$^{f/y}$*;Cre* and *Stag2*$^{f/y}$ forebrains. As revealed by clusters in the t-SNE plot, the two genotype groups had similar cellular compositions (Figure 4A,B). All cell clusters were present in *Stag2*$^{f/y}$*;Cre* brains, indicating generally normal neural cell differentiation. Cell-type identities were discovered with feature gene expression (Figure S5A). The OL lineage consisted of five clusters: cycling OL progenitors (OPCcycs), OL progenitors (OPCs), newly formed OLs (NFOLs), myelin-forming OLs (mFOLs), and fully matured OLs (MOLs). Quantification of the distributions of these five cell types within the OL lineage revealed a mild reduction in the number of MOLs in *Stag2*$^{f/y}$ forebrains (Figure 4C). We noticed that a higher percentage of neurons was recovered in the *Stag2*$^{f/y}$*;Cre* group. Since the bulk RNA-seq results did not show global upregulation of neuron-specific genes, we suspect that neurons in *Stag2*$^{f/y}$*;Cre* had fewer myelin-wrapped axons and were easier to be dissociated and kept alive during our library preparation for scRNA-seq. Thus, from the transcriptome analysis, we did not observe overt defects in most neural cell differentiation in the *Stag2*-deficient forebrain regions.

We then performed trajectory inference and pseudotime analysis of the OL lineage (Figure S5B,C). Consistent with our cell-type assignment, pseudotime variables indicated continuous

differentiation from OPCs to NFOLs, mFOLs, and MOLs (Figure S5D,E). The re-clustering of single cells in the OL lineage along the pseudotime path revealed that more cells were present in the terminal maturation stages in the *Stag2*$^{f/y}$ brains (Figure S5F,G). Conversely, more cells were retained at the undifferentiated stages in the *Stag2*$^{f/y}$*;Cre* brains. Strikingly, some myelination genes, including *Mal*, were specifically repressed in *Stag2*$^{f/y}$*;Cre* MOLs, with their expression in non-neural cells unaltered (Figures 4D and S6A). These observations suggest that STAG2 deficiency delays the maturation of OLs and compromises myelination-specific gene expression in mature OLs. Interestingly, compared to *Stag2* and genes encoding other cohesin core subunits, *Stag1* transcripts are less abundant in the OL lineage, except for cycling OPCs (Figure S6B,C). The low expression of *Stag1* in mature OLs might make these cells more dependent on *Stag2* for function.

To confirm the transcriptional defects in the OL lineage caused by *Stag2* deletion, we isolated primary OLs at intermediate differentiation stages from *Stag2*$^{f/y}$*;Cre* and *Stag2*$^{f/y}$ forebrains with antibody-conjugated magnetic beads and conducted bulk RNA-seq analysis (Figure 4E). For both genotypes, the marker genes for NFOL and mFOLs were highly expressed in the isolated primary OLs (Figure S7A), suggesting that they mainly contained these two cell types. In *Stag2*-deleted OLs, 271 and 292 genes were downregulated or upregulated by more than two folds, respectively (Figure 4F). The top canonical pathway enriched in these DEGs was the cholesterol biosynthesis pathway (Figure 4G). Intriguingly, the downregulated genes were generally highly expressed in WT cells, whereas the upregulated genes had low expression levels in WT cells (Figure S7B-D). Among the 105 downregulated DEGs identified by RNA-seq analysis of the whole brain of *Stag2*-deficient mice, 42 were also differentially expressed in primary oligodendrocytes (Figure 4H). The cholesterol biosynthesis pathways were recognized as

the major altered pathways (Figure S7E). Thus, defective cholesterol biosynthesis likely underlies hypomyelination and neurological defects in *Stag2* cKO mice.

We performed chromatin immunoprecipitation sequencing (ChIP-seq) experiments to examine the enrichment of the active transcription mark H3K27ac in *Stag2*$^{f/y}$ and *Stag2*$^{f/y}$*;Cre* OLs and found that *Stag2* loss did not appreciably affect H3K27Ac enrichment at transcription start sites (TSS) (Figure S8A,B). Consistent with our RNA-seq results, the upregulated genes had much lower H3K27ac enrichment near their TSS, indicating that they were less active. We then checked the genomic distribution of STAG2 by ChIP-seq. Among other genomic loci, STAG2 was enriched at TSS of stable and downregulated genes, including genes in the cholesterol biosynthesis pathways (Figure S8C,D). It was enriched at the TSS of upregulated genes to a lesser extent, suggesting that *Stag2* loss might have indirectly affected the expression of these less active genes.

Stag2 deletion does not alter compartments or TADs in OLs

To investigate whether chromosome conformation was altered by *Stag2* deletion and whether that caused transcription dysregulation, we performed high-dimensional chromosome conformational capture (Hi-C) analysis of primary OLs isolated from *Stag2*$^{f/y}$ and *Stag2*$^{f/y}$*;Cre* mice. We observed few compartment switching events in *Stag2*-deleted cells (Figure 5A-C and S9A-C). Virtually all genomic regions in *Stag2*-deleted cells were kept in their original compartment categories (AA or BB) (Figure 5C). Only a very small number of genomic regions switched compartments (AB or BA). Consistent with the RNA-seq data, analysis of average gene expression changes of DEGs in these genomic regions revealed that more genes located in the transcriptionally active A compartment (AA) were repressed in *Stag2*-deleted cells and more genes in the transcriptionally silent B compartment (BB) were upregulated (Figure 5D and S9D). Genes that switched from the

A compartment to the B compartment were not more repressed compared to those that remained in the A compartment. Likewise, compared to genes that stayed in the B compartment, genes located in chromatin regions that switched from compartment B to A were not significantly activated. Acute depletion of all forms of cohesin eliminates TAD formation (Wutz et al., 2017). In contrast, deletion of *Stag2* had minimal impact on TAD formation in oligodendrocytes (Figure 5E-H, S9E,F), suggesting that STAG1-cohesin compensates for the loss of STAG2-cohesin in spatial organization of chromatin at larger than megabase scales. Therefore, our findings are inconsistent with compartment switching and TAD alterations being the underlying cause for the observed gene expression changes in STAG2-deficient OLs.

Promoter-anchored loops were reduced in *Stag2*-deleted OLs

While TAD boundaries are largely conserved among species and cell types, chromatin interactions within each TAD are more flexible and variable in cells undergoing differentiation, tumorigenesis, and reprogramming (Dixon et al., 2015; Dixon et al., 2012). Among the intra-TAD chromatin interactions, the enhancer-promoter loops are particularly important for transcription and are often cell-type specific. We examined whether chromatin loops in OLs were affected by *Stag2* loss. Compared to *Stag2*$^{f/y}$ OLs, *Stag2*$^{f/y}$*;Cre* OLs had significantly fewer loops across almost all genomic distances (Figure 6A,B and S10). Loops specific to *Stag2*$^{f/y}$*;Cre* OLs, which were likely mediated by STAG1-cohesin, were longer than STAG2-dependent *Stag2*$^{f/y}$-specific loops. When genomic distances exceeded 0.25 Mb, the loops from *Stag2*$^{f/y}$*;Cre* cells gradually gained higher scores over loops from *Stag2*$^{f/y}$ cells (Figure 6C). Therefore, STAG1-cohesin cannot completely compensate for STAG2-cohesin during loop formation. STAG1-cohesin-mediated loops are

relatively longer than STAG2-cohesin-mediated loops, consistent with published findings in HeLa cells (Wutz et al., 2020).

We then tested whether the loop number decrease in *Stag2*-deficient cells could be a cause for transcriptional changes. When examining the local Hi-C maps, we noticed that loops anchored at gene promoters, including those of downregulated genes, were reduced in *Stag2*$^{f/y}$*;Cre* oligodendrocytes (Figure 6D and S11). Promoter-anchored loops (P-loops) can potentially be promoter-promoter links, promoter-enhancer links, and gene loops. The total number of P-loops was proportionally decreased in *Stag2*$^{f/y}$*;Cre* cells (Figure S12A). Moreover, the loops anchored at the downregulated genes were stronger than those at upregulated and stable genes (Figure S12B). We then compared P-loops associated with DEGs using pileup analysis of local contact maps. Loop enrichment at promoters of downregulated genes was reduced in *Stag2*$^{f/y}$*;Cre* cells to a greater extent than that at promoters of upregulated and stable genes (Figure 6E). Taken together, our results suggest that *Stag2* loss diminishes short chromosome loops, including promoter-anchored loops. Highly expressed genes might be more reliant on these loops for transcription and are preferentially downregulated by *Stag2* loss.

We also performed pileup analysis of local chromatin regions flanking transcription start sites (TSS) (Figure 6F). Strikingly, we observed a clear stripe that extended from the TSS of downregulated gene only in the direction of transcription. The formation of promoter-anchored stripes (P-stripes) on aggregated plots is consistent with one-sided loop extrusion from the promoter to the gene body. The P-stripe was still present in *Stag2*$^{f/y}$*;Cre* cells, suggesting that STAG1 could compensate for the loss of STAG2 and mediate its formation (Figure 6F and S12C).

DISCUSSION

Cohesin is critical for the three-dimensional (3D) organization of the genome by extruding chromosome loops. Acute depletion of cohesin abolishes chromosome loops and TADs, but has moderate effects on transcription. The two forms of cohesin in vertebrate somatic cells, namely STAG1-cohesin and STAG2-cohesin, have largely redundant functions in supporting sister-chromatid cohesion and cell viability, but they have non-redundant functions during development. In this study, we have established a myelination-promoting function of STAG2 in the central nervous system (CNS) in the mouse. We further provide evidence linking hypomyelination caused by STAG2 loss to reduced promoter-anchored loops at myelination genes in oligodendrocytes.

Myelination functions of STAG2 and implications for cohesinopathy

Selective ablation of *Stag2* in the nervous system in the mouse causes growth retardation, neurological defects, and premature death. STAG2 loss delays the maturation of oligodendrocytes and reduces the expression of highly active myelin and cholesterol biosynthesis genes in oligodendrocytes, resulting in hypomyelination in the CNS. Hypomyelination disorders in humans and mice are known to produce abnormal neurological behaviors similar to those seen in our *Stag2* cKO mice, suggesting that hypomyelination is a major underlying cause for the phenotypes in *Stag2* cKO mice. The growth retardation in these mice can be explained by insufficient secretion of growth hormones, which may be a consequence of defective neuronal signaling.

Mutations of cohesin subunits and regulators, including STAG2, cause the Cornelia de Lange syndrome (CdLS) and other similar developmental diseases, collectively termed cohesinopathy. CdLS patients exhibit short stature and developmental defects in multiple tissues

and organs, including the brain. Although STAG2 mutations are implicated in human cohesinopathy, these mutations are rare and hypomorphic (Soardi et al., 2017). The cohesin loader NIPBL is the most frequently mutated cohesin regulator in cohesinopathy (Mannini et al., 2013). NIPBL deficiency is expected to affect the functions of both STAG1- and STAG2-cohesin. It is possible that the partial loss of STAG2-cohesin function leads to subtle myelination defects in patients with cohesinopathy. Indeed, lack of myelination in certain brain regions of CdLS patients has been reported (Avagliano et al., 2017; Vuilleumier et al., 2002). As myelination of the CNS mostly occurs after birth and during childhood, strategies aimed at enhancing myelination might help to alleviate certain disease phenotypes and symptoms.

Mechanisms by which STAG2 promotes myelination

STAG2 promotes oligodendrocyte maturation and the expression of myelination genes in mature oligodendrocytes. Because STAG2 does not have an established cohesin-independent function, it most likely activates the myelination-promoting transcriptional program as a core component of cohesin. Consistent with previous reports (Rao et al., 2017), loss of STAG2-cohesin in oligodendrocytes does not affect genome compartmentalization, but reduces the number of relatively short chromosome loops, including promoter-anchored loops. Promoter-anchored loops at downregulated genes are reduced to a greater extent than those at stable and upregulated genes. These findings suggest that STAG2-cohesin promotes the myelination transcriptional program by forming promoter-anchored loops.

Pileup analysis of Hi-C maps reveals the formation of asymmetric promoter-anchored stripes in the direction of transcription at downregulated genes, indicative of active loading of cohesin at transcription start sites followed by one-sided loop extrusion from the promoter to the

gene body. The stripes are, however, not reduced in STAG2-deficient cells. Because both forms of cohesin are capable of loop extrusion, it is possible that STAG1-cohesin can compensate for the loss of STAG2-cohesin in loop extrusion. It remains to be tested whether the intrinsic kinetics and processivity of loop extrusion mediated by the two forms of cohesin are differentially regulated by cellular factors or posttranslational modifications and whether these differences contribute to their non-redundant roles in transcription regulation.

We envision three possibilities that may account for why oligodendrocytes, but not other cell types, are more severely affected by *Stag2* loss in the CNS. First, STAG2-cohesin may be more abundant than STAG1-cohesin in post-mitotic OLs, making them more dependent on STAG2 for proper functions. Second, STAG1-cohesin preferentially localizes to CTCF-enriched TAD boundaries whereas STAG2-cohesin is more enriched at enhancers lacking CTCF (Kojic et al., 2018). Enhancers are critical for cell-type-specific gene transcriptional programs. To cooperate with the axonal growth during postnatal neurodevelopment, enhancer-enriched transcription factors induce timely and robust gene expression in oligodendrocytes for proper myelination (Mitew et al., 2014). The high-demand for enhancer function may render the transcription of myelination genes more reliant on STAG2-cohesin. Finally, the C-terminal regions of STAG1 and STAG2 are divergent in sequence and may bind to different interacting proteins and be subjected to differential regulation. STAG2 may interact with oligodendrocyte-specific transcription factors and be preferentially recruited to myelination genes. It will be interesting to investigate the interactomes of STAG1 and STAG2 in oligodendrocytes using mass spectrometry.

STAG2-mediated chromosome looping and transcription

The mechanisms by which STAG2-dependent chromosome looping facilitates transcription are unclear at present. We propose several models that are not mutually exclusive (Figure 7). First, by forming promoter-enhancer loops, STAG2-cohesin brings the mediator complex and other enhancer-binding factors to the spatial proximity of the general transcriptional machinery at the promoter, thereby enhancing RNA polymerase II recruitment and transcription initiation. The existence of P stripes at STAG2-dependent genes in the Hi-C maps suggests that STAG2-mediated promoter-enhancer loops may involve enhancers located in the gene body. Second, loop extrusion by STAG2-cohesin may promote transcription elongation by regulating transcription-coupled pre-mRNA processing. For example, STAG2 has been shown to interact with RNA-DNA hybrid structures termed R-loops *in vitro* and in cells (Pan et al., 2020; Porter et al., 2021). R-loops formed between the nascent pre-mRNA and the DNA template impede transcription elongation and need to be suppressed (Moore and Proudfoot, 2009). When traveling with the transcription machinery on DNA, STAG2-cohesin might directly suppress R-loop formation or recruit other factors, such as the spliceosome, for co-transcriptional pre-mRNA processing and R-loop resolution. Third, STAG2-cohesin may establish promoter-terminator gene loops to recycle the RNA polymerase II that has finished one cycle of transcription back to the transcription start site for another round of transcription. Future experiments using high-resolution Hi-C methods in oligodendrocytes will allow us to better define the nature of STAG2-dependent promoter-anchored loops and stripes. It will also be interesting to examine whether *Stag2* deletion causes the accumulation of R-loops in downregulated genes and the incomplete splicing of their pre-mRNAs.

CONCLUSION

We have discovered a requirement for the cohesin subunit STAG2 in the myelination of the central nervous system in mammals. Our findings implicate hypomyelination as a contributing factor to certain phenotypes of cohesinopathy, including growth retardation and neurological disorders. We provide evidence to suggest that STAG2 promotes the myelination transcriptional program in oligodendrocytes through the formation of promoter-anchored loops. Our study establishes oligodendrocytes as a physiologically relevant cell system for dissecting the cellular functions and regulatory mechanisms of cohesin-mediated chromosome folding and genome organization.

STAR★METHODS

Detailed methods are provided in the online version of this paper and include the following:

- KEY RESOURCES TABLE
- RESOURCE AVAILABILITY
  - Lead contact
  - Materials availability
  - Data and code availability
- EXPERIMENTAL MODEL AND SUBJECT DETAILS
  - Generation of *Stag2*$^{f/f}$ and *Stag2*$^{f/y}$ mice and mouse husbandry
- METHOD DETAILS
  - Immunoblotting
  - Tissue histology and immunohistochemistry
  - Isolation of primary oligodendrocytes
  - TSE Metabolic cage analysis
  - Growth hormone and IGF-1 detection
  - Sterol and oxysterol composition analysis
  - Electron microscopy
  - Generation of RNA-seq libraries and sequencing
  - Differential expression and pathway analysis
  - RT-qPCR analysis
  - Transcriptional profiling of brain cells
  - Chromatin immunoprecipitation followed by sequencing (ChIP-seq)
  - Hi-C library generation, sequencing, and analysis

- Chromosome loop analysis and integration with RNA-seq
- QUANTIFICATION AND STAITSTICAL ANALYSIS

SUPPLEMENTAL INFORMATION

Supplemental Information including Supplemental Figures 1-12 can be found online.

ACKNOWLEDGMENTS

We thank Sung Jun Bae for taking the mouse photos and John Shelton for help with histology and *in situ* hybridization. We are grateful to Jeffrey McDonald for the sterol composition analysis, Richard Lu and Lu Sun for providing reagents and advice for oligodendrocytes isolation, and Applied Bioinformatics Laboratories at NYU Langone Health for the Hi-C analysis. We also thank the Yu lab members for helpful discussions and for reading the manuscript critically. This study was supported by the Cancer Prevention and Research Institute of Texas (CPRIT) (RP160667-P2) and the Welch foundation (I-1441).

AUTHOR CONTRIBUTIONS

N.C. and H.Y. conceived and designed the study. N.C. performed all the experiments. M.K., N.C., and C. X. performed the analysis and interpretation of NGS data. N.C. and B.M.E. performed histology and EM image analysis. N.C. and H.Y. wrote the manuscript with input from all authors. H.Y. supervised the project. All authors approved the manuscript.

DECLARATION OF INTERESTS

The authors declare no competing interests.

REFERENCES

.

Andrews, S. (2010). FastQC: a quality control tool for high throughput sequence data.

Avagliano, L., Grazioli, P., Mariani, M., Bulfamante, G.P., Selicorni, A., and Massa, V. (2017). Integrating molecular and structural findings: Wnt as a possible actor in shaping cognitive impairment in Cornelia de Lange syndrome. Orphanet J. Rare Dis. *12*, 174.

Ay, F., Bailey, T.L., and Noble, W.S. (2014). Statistical confidence estimation for Hi-C data reveals regulatory chromatin contacts. Genome Res *24*, 999-1011.

Butler, A., Hoffman, P., Smibert, P., Papalexi, E., and Satija, R. (2018). Integrating single-cell transcriptomic data across different conditions, technologies, and species. Nat Biotechnol *36*, 411-420.

Cahoy, J.D., Emery, B., Kaushal, A., Foo, L.C., Zamanian, J.L., Christopherson, K.S., Xing, Y., Lubischer, J.L., Krieg, P.A., Krupenko, S.A.*, et al.* (2008). A transcriptome database for astrocytes, neurons, and oligodendrocytes: a new resource for understanding brain development and function. J Neurosci *28*, 264-278.

Cao, J., Spielmann, M., Qiu, X., Huang, X., Ibrahim, D.M., Hill, A.J., Zhang, F., Mundlos, S., Christiansen, L., Steemers, F.J.*, et al.* (2019). The single-cell transcriptional landscape of mammalian organogenesis. Nature *566*, 496-502.

Choi, E., Zhang, X., Xing, C., and Yu, H. (2016). Mitotic Checkpoint Regulators Control Insulin Signaling and Metabolic Homeostasis. Cell *166*, 567-581.

Davidson, I.F., Bauer, B., Goetz, D., Tang, W., Wutz, G., and Peters, J.M. (2019). DNA loop extrusion by human cohesin. Science *366*, 1338-1345.

De Koninck, M., Lapi, E., Badia-Careaga, C., Cossio, I., Gimenez-Llorente, D., Rodriguez-Corsino, M., Andrada, E., Hidalgo, A., Manzanares, M., Real, F.X.*, et al.* (2020). Essential Roles

of Cohesin STAG2 in Mouse Embryonic Development and Adult Tissue Homeostasis. Cell Rep. *32*, 108014.

De Koninck, M., and Losada, A. (2016). Cohesin Mutations in Cancer. Cold Spring Harb Perspect Med *6*.

Dixon, J.R., Jung, I., Selvaraj, S., Shen, Y., Antosiewicz-Bourget, J.E., Lee, A.Y., Ye, Z., Kim, A., Rajagopal, N., Xie, W.*, et al.* (2015). Chromatin architecture reorganization during stem cell differentiation. Nature *518*, 331-336.

Dixon, J.R., Selvaraj, S., Yue, F., Kim, A., Li, Y., Shen, Y., Hu, M., Liu, J.S., and Ren, B. (2012). Topological domains in mammalian genomes identified by analysis of chromatin interactions. Nature *485*, 376-380.

Dobin, A., Davis, C.A., Schlesinger, F., Drenkow, J., Zaleski, C., Jha, S., Batut, P., Chaisson, M., and Gingeras, T.R. (2013). STAR: ultrafast universal RNA-seq aligner. Bioinformatics *29*, 15-21.

Dulken, B.W., Buckley, M.T., Navarro Negredo, P., Saligrama, N., Cayrol, R., Leeman, D.S., George, B.M., Boutet, S.C., Hebestreit, K., Pluvinage, J.V.*, et al.* (2019). Single-cell analysis reveals T cell infiltration in old neurogenic niches. Nature *571*, 205-210.

Durand, N.C., Shamim, M.S., Machol, I., Rao, S.S., Huntley, M.H., Lander, E.S., and Aiden, E.L. (2016). Juicer Provides a One-Click System for Analyzing Loop-Resolution Hi-C Experiments. Cell Syst. *3*, 95-98.

Flores-Obando, R.E., Freidin, M.M., and Abrams, C.K. (2018). Rapid and Specific Immunomagnetic Isolation of Mouse Primary Oligodendrocytes. J. Vis. Exp.

Flyamer, I.M., Illingworth, R.S., and Bickmore, W.A. (2020). Coolpup.py: versatile pile-up analysis of Hi-C data. Bioinformatics *36*, 2980-2985.

Giusti, S.A., Vercelli, C.A., Vogl, A.M., Kolarz, A.W., Pino, N.S., Deussing, J.M., and Refojo, D. (2014). Behavioral phenotyping of Nestin-Cre mice: implications for genetic mouse models of psychiatric disorders. J. Psychiatr. Res. *55*, 87-95.

Haarhuis, J.H., Elbatsh, A.M., and Rowland, B.D. (2014). Cohesin and its regulation: on the logic of X-shaped chromosomes. Dev. Cell *31*, 7-18.

Haarhuis, J.H.I., van der Weide, R.H., Blomen, V.A., Yanez-Cuna, J.O., Amendola, M., van Ruiten, M.S., Krijger, P.H.L., Teunissen, H., Medema, R.H., van Steensel, B.*, et al.* (2017). The Cohesin Release Factor WAPL Restricts Chromatin Loop Extension. Cell *169*, 693-707 e614.

Hara, K., Zheng, G., Qu, Q., Liu, H., Ouyang, Z., Chen, Z., Tomchick, D.R., and Yu, H. (2014). Structure of cohesin subcomplex pinpoints direct shugoshin-Wapl antagonism in centromeric cohesion. Nat. Struct. Mol. Biol. *21*, 864-870.

Heinz, S., Benner, C., Spann, N., Bertolino, E., Lin, Y.C., Laslo, P., Cheng, J.X., Murre, C., Singh, H., and Glass, C.K. (2010). Simple combinations of lineage-determining transcription factors prime cis-regulatory elements required for macrophage and B cell identities. Mol. Cell *38*, 576-589.

Hubler, Z., Allimuthu, D., Bederman, I., Elitt, M.S., Madhavan, M., Allan, K.C., Shick, H.E., Garrison, E., M, T.K., Factor, D.C.*, et al.* (2018). Accumulation of 8,9-unsaturated sterols drives oligodendrocyte formation and remyelination. Nature *560*, 372-376.

Kim, Y., Shi, Z., Zhang, H., Finkelstein, I.J., and Yu, H. (2019). Human cohesin compacts DNA by loop extrusion. Science *366*, 1345-1349.

Kojic, A., Cuadrado, A., De Koninck, M., Gimenez-Llorente, D., Rodriguez-Corsino, M., Gomez-Lopez, G., Le Dily, F., Marti-Renom, M.A., and Losada, A. (2018). Distinct roles of

cohesin-SA1 and cohesin-SA2 in 3D chromosome organization. Nat. Struct. Mol. Biol. *25*, 496-504.

Langmead, B., and Salzberg, S.L. (2012). Fast gapped-read alignment with Bowtie 2. Nat. Methods *9*, 357-359.

Lazaris, C., Kelly, S., Ntziachristos, P., Aifantis, I., and Tsirigos, A. (2017). HiC-bench: comprehensive and reproducible Hi-C data analysis designed for parameter exploration and benchmarking. BMC Genomics *18*, 22.

Li, Y., Haarhuis, J.H.I., Sedeno Cacciatore, A., Oldenkamp, R., van Ruiten, M.S., Willems, L., Teunissen, H., Muir, K.W., de Wit, E., Rowland, B.D.*, et al.* (2020). The structural basis for cohesin-CTCF-anchored loops. Nature *578*, 472-476.

Liao, Y., Smyth, G.K., and Shi, W. (2014). featureCounts: an efficient general purpose program for assigning sequence reads to genomic features. Bioinformatics *30*, 923-930.

Liu, X., Zhang, Y., Chen, Y., Li, M., Zhou, F., Li, K., Cao, H., Ni, M., Liu, Y., Gu, Z.*, et al.* (2017). In Situ Capture of Chromatin Interactions by Biotinylated dCas9. Cell *170*, 1028-1043 e1019.

Lopez-Delisle, L., Rabbani, L., Wolff, J., Bhardwaj, V., Backofen, R., Gruning, B., Ramirez, F., and Manke, T. (2020). pyGenomeTracks: reproducible plots for multivariate genomic data sets. Bioinformatics.

Luecken, M.D., and Theis, F.J. (2019). Current best practices in single-cell RNA-seq analysis: a tutorial. Mol Syst Biol *15*, e8746.

Mannini, L., Cucco, F., Quarantotti, V., Krantz, I.D., and Musio, A. (2013). Mutation spectrum and genotype-phenotype correlation in Cornelia de Lange syndrome. Hum. Mutat. *34*, 1589-1596.

Marques, S., van Bruggen, D., Vanichkina, D.P., Floriddia, E.M., Munguba, H., Varemo, L., Giacomello, S., Falcao, A.M., Meijer, M., Bjorklund, A.K., *et al.* (2018). Transcriptional Convergence of Oligodendrocyte Lineage Progenitors during Development. Dev. Cell *46*, 504-517 e507.

Marques, S., Zeisel, A., Codeluppi, S., van Bruggen, D., Mendanha Falcao, A., Xiao, L., Li, H., Haring, M., Hochgerner, H., Romanov, R.A., *et al.* (2016). Oligodendrocyte heterogeneity in the mouse juvenile and adult central nervous system. Science *352*, 1326-1329.

Martincorena, I., and Campbell, P.J. (2015). Somatic mutation in cancer and normal cells. Science *349*, 1483-1489.

Marton, R.M., Miura, Y., Sloan, S.A., Li, Q., Revah, O., Levy, R.J., Huguenard, J.R., and Pasca, S.P. (2019). Differentiation and maturation of oligodendrocytes in human three-dimensional neural cultures. Nat. Neurosci. *22*, 484-491.

Mathys, H., Davila-Velderrain, J., Peng, Z., Gao, F., Mohammadi, S., Young, J.Z., Menon, M., He, L., Abdurrob, F., Jiang, X., *et al.* (2019). Single-cell transcriptomic analysis of Alzheimer's disease. Nature *570*, 332-337.

McDonald, J.G., Smith, D.D., Stiles, A.R., and Russell, D.W. (2012). A comprehensive method for extraction and quantitative analysis of sterols and secosteroids from human plasma. J. Lipid Res. *53*, 1399-1409.

Mitew, S., Hay, C.M., Peckham, H., Xiao, J., Koenning, M., and Emery, B. (2014). Mechanisms regulating the development of oligodendrocytes and central nervous system myelin. Neuroscience *276*, 29-47.

Moore, M.J., and Proudfoot, N.J. (2009). Pre-mRNA processing reaches back to transcription and ahead to translation. Cell *136*, 688-700.

Pan, H., Jin, M., Ghadiyaram, A., Kaur, P., Miller, H.E., Ta, H.M., Liu, M., Fan, Y., Mahn, C., Gorthi, A.*, et al.* (2020). Cohesin SA1 and SA2 are RNA binding proteins that localize to RNA containing regions on DNA. Nucleic Acids Res. *48*, 5639-5655.

Piche, J., Van Vliet, P.P., Puceat, M., and Andelfinger, G. (2019). The expanding phenotypes of cohesinopathies: one ring to rule them all! Cell Cycle *18*, 2828-2848.

Porter, H., Li, Y., Varsally, W., Neguembor, M.V., Beltran, M., Pezic, D., Martin, L., Cornejo, M.T., Bhamra, A., Surinova, S.*, et al.* (2021). STAG proteins promote cohesin ring loading at R-loops. bioRxiv, 2021.2002.2020.432055.

Rao, S.S.P., Huang, S.C., Glenn St Hilaire, B., Engreitz, J.M., Perez, E.M., Kieffer-Kwon, K.R., Sanborn, A.L., Johnstone, S.E., Bascom, G.D., Bochkov, I.D.*, et al.* (2017). Cohesin Loss Eliminates All Loop Domains. Cell *171*, 305-320 e324.

Remeseiro, S., Cuadrado, A., Carretero, M., Martinez, P., Drosopoulos, W.C., Canamero, M., Schildkraut, C.L., Blasco, M.A., and Losada, A. (2012). Cohesin-SA1 deficiency drives aneuploidy and tumourigenesis in mice due to impaired replication of telomeres. EMBO J. *31*, 2076-2089.

Remeseiro, S., Cuadrado, A., Kawauchi, S., Calof, A.L., Lander, A.D., and Losada, A. (2013a). Reduction of Nipbl impairs cohesin loading locally and affects transcription but not cohesion-dependent functions in a mouse model of Cornelia de Lange Syndrome. Biochim. Biophys. Acta *1832*, 2097-2102.

Remeseiro, S., Cuadrado, A., and Losada, A. (2013b). Cohesin in development and disease. Development *140*, 3715-3718.

Robinson, M.D., McCarthy, D.J., and Smyth, G.K. (2010). edgeR: a Bioconductor package for differential expression analysis of digital gene expression data. Bioinformatics *26*, 139-140.

Ross-Innes, C.S., Stark, R., Teschendorff, A.E., Holmes, K.A., Ali, H.R., Dunning, M.J., Brown, G.D., Gojis, O., Ellis, I.O., Green, A.R., *et al.* (2012). Differential oestrogen receptor binding is associated with clinical outcome in breast cancer. Nature *481*, 389-393.

Saher, G., Brugger, B., Lappe-Siefke, C., Mobius, W., Tozawa, R., Wehr, M.C., Wieland, F., Ishibashi, S., and Nave, K.A. (2005). High cholesterol level is essential for myelin membrane growth. Nat. Neurosci. *8*, 468-475.

Saunders, A., Macosko, E.Z., Wysoker, A., Goldman, M., Krienen, F.M., de Rivera, H., Bien, E., Baum, M., Bortolin, L., Wang, S., *et al.* (2018). Molecular Diversity and Specializations among the Cells of the Adult Mouse Brain. Cell *174*, 1015-1030 e1016.

Schwarzer, W., Abdennur, N., Goloborodko, A., Pekowska, A., Fudenberg, G., Loe-Mie, Y., Fonseca, N.A., Huber, W., Haering, C.H., Mirny, L., *et al.* (2017). Two independent modes of chromatin organization revealed by cohesin removal. Nature *551*, 51-56.

Shi, Z., Gao, H., Bai, X.C., and Yu, H. (2020). Cryo-EM structure of the human cohesin-NIPBL-DNA complex. Science *368*, 1454-1459.

Soardi, F.C., Machado-Silva, A., Linhares, N.D., Zheng, G., Qu, Q., Pena, H.B., Martins, T.M.M., Vieira, H.G.S., Pereira, N.B., Melo-Minardi, R.C., *et al.* (2017). Familial STAG2 germline mutation defines a new human cohesinopathy. NPJ Genom. Med. *2*, 7.

Stuart, T., Butler, A., Hoffman, P., Hafemeister, C., Papalexi, E., Mauck, W.M., 3rd, Hao, Y., Stoeckius, M., Smibert, P., and Satija, R. (2019). Comprehensive Integration of Single-Cell Data. Cell *177*, 1888-1902 e1821.

Thakurela, S., Garding, A., Jung, R.B., Muller, C., Goebbels, S., White, R., Werner, H.B., and Tiwari, V.K. (2016). The transcriptome of mouse central nervous system myelin. Sci. Rep. *6*, 25828.

Tronche, F., Kellendonk, C., Kretz, O., Gass, P., Anlag, K., Orban, P.C., Bock, R., Klein, R., and Schutz, G. (1999). Disruption of the glucocorticoid receptor gene in the nervous system results in reduced anxiety. Nat. Genet. *23*, 99-103.

Tsirigos, A., Haiminen, N., Bilal, E., and Utro, F. (2012). GenomicTools: a computational platform for developing high-throughput analytics in genomics. Bioinformatics *28*, 282-283.

Uhlmann, F. (2016). SMC complexes: from DNA to chromosomes. Nat. Rev. Mol. Cell Biol. *17*, 399-412.

van Tilborg, E., van Kammen, C.M., de Theije, C.G.M., van Meer, M.P.A., Dijkhuizen, R.M., and Nijboer, C.H. (2017). A quantitative method for microstructural analysis of myelinated axons in the injured rodent brain. Sci. Rep. *7*, 16492.

Vian, L., Pekowska, A., Rao, S.S.P., Kieffer-Kwon, K.R., Jung, S., Baranello, L., Huang, S.C., El Khattabi, L., Dose, M., Pruett, N.*, et al.* (2018). The Energetics and Physiological Impact of Cohesin Extrusion. Cell *175*, 292-294.

Vuilleumier, N., Kovari, E., Michon, A., Hof, P.R., Mentenopoulos, G., Giannakopoulos, P., and Bouras, C. (2002). Neuropathological analysis of an adult case of the Cornelia de Lange syndrome. Acta Neuropathol. *104*, 327-332.

Williamson, J.M., and Lyons, D.A. (2018). Myelin Dynamics Throughout Life: An Ever-Changing Landscape? Front. Cell Neurosci. *12*, 424.

Wingett, S. (2011). FastQ Screen: quality control tool to screen a library of sequences in FastQ format against a set of sequence databases. .

Wolf, N.I., Ffrench-Constant, C., and van der Knaap, M.S. (2021). Hypomyelinating leukodystrophies - unravelling myelin biology. Nat. Rev. Neurol. *17*, 88-103.

Wutz, G., Ladurner, R., St Hilaire, B.G., Stocsits, R.R., Nagasaka, K., Pignard, B., Sanborn, A., Tang, W., Varnai, C., Ivanov, M.P., *et al.* (2020). ESCO1 and CTCF enable formation of long chromatin loops by protecting cohesin(STAG1) from WAPL. eLife *9*.

Wutz, G., Varnai, C., Nagasaka, K., Cisneros, D.A., Stocsits, R.R., Tang, W., Schoenfelder, S., Jessberger, G., Muhar, M., Hossain, M.J., *et al.* (2017). Topologically associating domains and chromatin loops depend on cohesin and are regulated by CTCF, WAPL, and PDS5 proteins. EMBO J. *36*, 3573-3599.

Yatskevich, S., Rhodes, J., and Nasmyth, K. (2019). Organization of Chromosomal DNA by SMC Complexes. Annu. Rev. Genet. *53*, 445-482.

Zeisel, A., Hochgerner, H., Lonnerberg, P., Johnsson, A., Memic, F., van der Zwan, J., Haring, M., Braun, E., Borm, L.E., La Manno, G., *et al.* (2018). Molecular Architecture of the Mouse Nervous System. Cell *174*, 999-1014 e1022.

Zhang, Y., Liu, T., Meyer, C.A., Eeckhoute, J., Johnson, D.S., Bernstein, B.E., Nusbaum, C., Myers, R.M., Brown, M., Li, W., *et al.* (2008). Model-based analysis of ChIP-Seq (MACS). Genome Biol. *9*, R137.

Zheng, G., and Yu, H. (2015). Regulation of sister chromatid cohesion during the mitotic cell cycle. Sci. China Life Sci. *58*, 1089-1098.

Zywitza, V., Misios, A., Bunatyan, L., Willnow, T.E., and Rajewsky, N. (2018). Single-Cell Transcriptomics Characterizes Cell Types in the Subventricular Zone and Uncovers Molecular Defects Impairing Adult Neurogenesis. Cell Rep. *25*, 2457-2469 e2458.

METHODS

KEY RESOURCES TABLE

RESOURCE AVAILABILITY

Lead contact

Further information and requests for resources and reagents should be directed to and will be fulfilled by the Lead Contact, Hongtao Yu (yuhongtao@westlake.edu.cn).

Material availability

Unique materials generated in this study will be available upon request.

Data and code availability

The RNA-seq, scRNA-seq, ChIP-seq, and Hi-C datasets generated and analyzed during the current study are available in the GEO repository, with the accession number xxx. Relevant code is available from the corresponding author upon request.

EXPERIMENTAL MODEL AND SUBJECT DETAILS

Generation of *Stag2*$^{f/f}$ and *Stag2*$^{f/y}$ mice and mouse husbandry. The *STAG2* locus was targeted by inserting one neo cassette and two loxP sites flanking exon 8 via homologous recombination in the mouse embryonic stem (ES) cells. G418-selected positive ES clones were screened for successful targeting by nested PCR tests on both 5' and 3' integration sites of loxP. Four confirmed ES clones were then microinjected into mouse blastocysts. The chimeras were bred to the R26FLP mouse line for the removal of the neo cassette. *Stag2*$^{f/+}$ mice with the 129/B6 background were were crossed with *Stag2*$^{f/y}$ or wildtype C57BL/6J mice and maintained on this background. For

the generation of the central nervous system-specific *Stag2*$^{f/y}$*;Cre* mice, the *Stag2*$^{f/f}$ mice were crossed with the transgenic mice carrying one allele of *Cre* driven by the rat nestin promoter and enhancer (Tg(Nes-cre)1Kln, JAX stock #003771) (Giusti et al., 2014; Tronche et al., 1999).

All animals were handled in accordance with institutional guidelines of the Institutional Animal Care and Use Committee of University of Texas (UT) Southwestern Medical Center. All mice were housed in the antigen-free barrier facility with 12 hr light/dark cycles (6 AM on and 6 PM off). Mice were fed a standard rodent chow (2016 Teklad Global 16% protein rodent diet, Harlan Laboratories).

METHOD DETAILS

Immunoblotting. The C-terminal fragment of human STAG2 protein was expressed and purified from *Escherichia coli* and used as the antigen to generate rabbit polyclonal antibodies against STAG2 at YenZym. Other antibodies were purchased from the following commercial sources: anti-SMC1 (Bethyl Laboratories, A300-055A), anti-SMC3 (Bethyl Laboratories, A300-060A), anti-RAD21 (Bethyl Laboratories, A300-080A), anti-SA1 (Bethyl Laboratories, A302-579A), anti-SA2 (Bethyl Laboratories, A302-581A), anti-α-TUBULIN (Sigma-Aldrich, DM1A), anti-MBP (Abcam, ab7349), anti-PLP1 (Abcam, ab28486), and anti-H3K27ac (Abcam, ab4729).

For immunoblotting, brain hemispheres were homogenized in a Precellys tissue homogenizer (Bertin Instruments) with the lysis buffer [20 mM Tris-HCl (pH 7.7), 137 mM NaCl, 2 mM EDTA, 10% (v/v) glycerol, 1% (v/v) TritonX-100, 0.5 mM dithiothreitol, 1 mM PMSF, 1 mM Na_3VO4, 10 mM β-glycerophosphate, 5 mM NaF and protease inhibitors (Roche)]. Homogenized brain tissues were lysed on ice for 1 hr. The lysate was then subjected to centrifugation at 20,817 g at 4°C for 20 min and further cleared by filtering through a 0.45 μm

filter. The cleared lysate was analyzed by SDS-PAGE and transferred to membranes, which was then incubated with the appropriate primary and secondary antibodies. The blots were imaged with the Odyssey Infrared Imaging System (LI-COR).

Tissue histology and immunohistochemistry. Mouse brains were fixed in 10% neutral buffered formalin solution for 48 hr followed by paraffin embedding and coronal or sagittal sectioning at 5 μm. Hematoxylin and eosin (H&E) staining and Luxol fast blue staining were performed by the Molecular Pathology Core at UT Southwestern Medical Center. Investigators were blinded to the genotype. Images were acquired with the DM2000 microscope (Leica) at 1.25X resolution.

Immunohistochemistry was performed as previously described (Choi et al., 2016). Briefly, deparaffinized sections were fixed with 4% paraformaldehyde, subjected to antigen retrieval by boiling with 10 mM sodium citrate (pH 6.0), and then incubated with the indicated antibodies at 1:100 dilution. The slides were scanned with an Axioscan.Z1 microscope (Zeiss) at 40X resolution at the Whole Brain Microscopy Facility at UT Southwestern Medical Center. Images were processed and quantified with Image J. For the myelinated fiber length measurement and coherency analysis, coronal sections of the brain cortex stained with the anti-MBP antibody were processed as previously described (van Tilborg et al., 2017). The myelinated axial thinning and fiber length measurement were performed by the plugin DiameterJ. The coherency analysis of myelinated axons was performed with the plugin OrientationJ.

Isolation of primary oligodendrocytes. The immunomagnetic isolation of oligodendrocytes from *Stag2*$^{f/y}$ and *Stag2*$^{f/y}$*;Cre* P12-P14 pups was conducted using anti-O4 microbeads (Miltenyi Biotec) according to a published protocol (Flores-Obando et al., 2018). Briefly, dissected brain

cortex was triturated in the papain dissociation solution with B-27 supplement. The single-cell suspension was incubated with anti-O4 magnetic beads and passed through a magnetic column to enrich oligodendrocytes. Freshly prepared oligodendrocytes were directly used or fixed for subsequent analysis.

Metabolic cage analysis. Mice were singly housed in shoebox-sized cages with a five-day acclimation period followed with a four-day recording period. Recorded parameters were analyzed by the TSE system and normalized to body weight. The experiments were conducted by the core personnel under the core protocol at the Metabolic Phenotyping Core at UT Southwestern Medical Center. Investigators were blinded to the genotype.

Growth hormone and IGF-1 detection. Blood samples were collected from facial bleeding without fasting. Plasma growth hormone levels were determined with the rat/mouse growth hormone ELISA kit (EMD Milipore, EZRMGH-45K). Plasma IGF-1 concentrations were measured using the mouse/rat IGF1 Quantikine ELISA kit (R&D Systems).

Sterol and oxysterol composition analysis. Brain hemispheres were pre-weighed and snap-frozen for extraction and measurement by mass spectrometry. The sterol extraction and quantitative analysis were conducted at the Center of Human Nutrition at UT Southwestern Medical Center as described previously (McDonald et al., 2012).

Electron microscopy. *Stag2*$^{f/y}$ and *Stag2*$^{f/y}$*;Cre* P18 pups were transcardially perfused with 4% paraformaldehyde, 1% glutaraldehyde in 0.1 M sodium cacodylate buffer (pH 7.4). Tissues were

dissected and fixed with 2.5% (v/v) glutaraldehyde in 0.1 M sodium cacodylate buffer (pH 7.4) for at least two hours. After three rinses with the 0.1 M sodium cacodylate buffer, optic nerve samples were embedded in 3% agarose and sliced into small blocks. All samples were again rinsed with the 0.1M sodium cacodylate buffer three times and post-fixed with 1% osmium tetroxide and 0.8 % potassium ferricyanide in the 0.1 M sodium cacodylate buffer for three hours at room temperature. Blocks were rinsed with water and *en bloc* stained with 4% uranyl acetate in 50% ethanol for two hours. Samples were dehydrated with increasing concentrations of ethanol, transitioned into propylene oxide, infiltrated with Embed-812 resin, and polymerized in a 60°C oven overnight. Blocks were sectioned with a diamond knife (Diatome) on a Leica Ultracut 7 ultramicrotome (Leica Microsystems) and collected onto copper grids, post-stained with 2% aqueous uranyl acetate and lead citrate. Images were acquired on a Tecnai G2 Spirit transmission electron microscope (Thermo Fischer) equipped with a LaB6 source using a voltage of 120 kV. Tissue processing, sectioning, and staining were completed by the Electron Microscopy Core at UT Southwestern Medical Center.

RNA-seq library preparation and sequencing. Total RNA was extracted from brain hemispheres or isolated oligodendrocytes with Trizol. RNA integrity was determined by the Agilent BioAnalyzer 2100. TruSeq Stranded mRNA library prep kit (Illumina) was used to generate the mRNA libraries. The libraries were analyzed by the Bioanalyzer and multiplexed and sequenced using the NextSeq 500 high output kit (400M reads) for the brain libraries or NextSeq 500 mid output kit (130M reads) for the isolated oligodendrocytes libraries at the Next Generation Sequencing Core at UT Southwestern Medical Center.

Differential expression and pathway analysis. Raw data from the sequencer were de-multiplexed and converted to fastq files using bcl2fastq (v2.17, Illumina). The fastq files were checked for quality using fastqc (v0.11.2) (Andrews, 2010) and fastq_screen (v0.4.4) (Wingett, 2011). Fastq files were mapped to the mm10 mouse reference genome (from iGenomes) using STAR (Dobin et al., 2013). Read counts were then generated using featureCounts (Liao et al., 2014). TMM normalization and differential expression analysis were performed using edgeR (Robinson et al., 2010). Pathway analysis was performed with the Ingenuity pathway analysis (IPA) software. Genes with more than 1.5-fold change and FDR < 0.01 were included in the brain RNA-seq pathway analysis. Genes with more than 2-fold change and FDR <0.05 were used for the pathway analysis of the RNA-seq data from oligodendrocytes.

RT-qPCR analysis. Single-stranded cDNAs were converted from 2 μg of total RNA extracted from mouse brains with the high-capacity cDNA reverse transcription kit (Applied Biosystems). Quantitative-PCR was conducted to determine transcript levels using gene-specific TaqMan probes (Applied Biosystems).

Single-cell RNA-seq. Single-cell suspension was prepared from forebrains of P13 *Stag2*$^{f/y}$ or *Stag2*$^{f/y}$*;Cre* pups using the Papain Dissociation System (Worthington Biochemical, LK003150) according to the manufacturer's instructions. Biological duplicates were made for each genotype. Single-cell RNA-seq libraries were generated with the Chromium Single Cell 3' GEM, Library & Gel Bead Kit v3 (10x Genomics) according to the manufacturer's guidelines. Cell density and viability were checked by the TC-20 Cell Counter (Bio-Rad). Cells were then loaded onto Chip B in the Chromium Controller (10x Genomics). 10,000 cells were targeted for each sample. The

libraries were analyzed by the Bioanalyzer (Agilent) and pair-end sequenced in two flowcells of the NextSeq 500 High Output (400M) run. The sequencing was performed at the Next Generation Sequencing Core at UT Southwestern Medical Center.

Data de-multiplexing and alignment was performed using the Cell Ranger pipeline (https://support.10xgenomics.com/single-cell-gene-expression/software/pipelines/latest/using/mkfastq) (10x Genomics). The raw features, barcodes, and matrixes were used as input for further analysis using the R package Seurat3 (Butler et al., 2018; Stuart et al., 2019) (https://satijalab.org/seurat/). Cells were filtered by the following criteria: nFeature_RNA (200-9500) and percent.mt < 10. After filtering, a total of 5,834 cells in *Stag2*$^{f/y}$*#1*, 4,699 cells in *Stag2*$^{f/y}$*#2*, 9,050 cells in *Stag2*$^{f/y}$*;Cre#1*, and 3,073 cells in *Stag2*$^{f/y}$*;Cre#2* were used for downstream analysis. 2,000 variable features were found from each normalized dataset. All datasets were then integrated using identified anchors (dims = 1:30). Standard scaling and principal component analysis (PCA), clustering (resolution = 0.5), and tSNE reduction (dims = 1:30) were performed on the integrated dataset. Cluster biomarkers were identified, and top features were examined. Clusters were then manually assigned to distinct cell type identities with knowledge from previous studies (Cahoy et al., 2008; Dulken et al., 2019; Marques et al., 2018; Marques et al., 2016; Marton et al., 2019; Saunders et al., 2018; Zeisel et al., 2018; Zywitza et al., 2018) (http://www.brainrnaseq.org/) (http://dropviz.org/). Clusters with the same cell type identities were merged. 5 clusters of oligodendrocyte lineage [cycling oligodendrocyte progenitors (OPCcycs), oligodendrocyte progenitors (OPCs), newly formed oligodendrocytes (NFOLs), myelin-forming oligodendrocytes (mFOLs) and fully matured oligodendrocytes (MFOLs)] were identified and selected for indicated gene expression comparison and plotting using Vlnplot or FeaturePlot functions. The trajectory analysis was performed using Monocle3

(Cao et al., 2019) in the oligodendrocyte cell population. Gene density plot over pseudotime was generated as previously described (Luecken and Theis, 2019).

ChIP-seq. Chromatin immunoprecipitation (ChIP) was performed as previously described (Liu et al., 2017). Briefly, isolated oligodendrocytes were fixed with 1% formaldehyde and fragmented with a sonicator (Branson 450). The fragmented chromatin was incubated with antibodies overnight at 4°C. Dynabeads Protein A (Thermo Fisher Scientific) was used for the immunoprecipitation. Libraries were generated by the Next Gen DNA Library Kit (Active Motif) with the Next Gen Indexing Kit (Active Motif) for STAG2 ChIP-seq or the KAPA HyperPrep Kits (KAPA Systems) for histone ChIP-seq. The libraries were analyzed by the Bioanalyzer and pool-sequenced with the NextSeq 500 mid output (130M) kit. After mapping reads to the mouse genome (mm10) by bowtie2 (v2.2.3) (Langmead and Salzberg, 2012) with the parameter "–sensitive", we performed filtering by removing alignments with mapping quality less than 10 and then removing duplicate reads identified by Picard MarkDuplicates (v1.127). For STAG2 ChIP-seq, Picard MarkDuplicate was used to remove duplicates together with options to use molecular identifiers (MIDs) information in the reads. Enriched regions (peaks) were identified using MACS2 (v2.0.10) (Zhang et al., 2008), with a q-value cut-off of 0.05 for peaks. Peak regions were annotated by HOMER(Ross-Innes et al., 2012).

Hi-C library generation, sequencing, and analysis. Hi-C was performed at the Genome Technology Center at NYU Langone Health from 3.5-4.0 μg of DNA isolated from cells cross-linked with 2% formaldehyde at room temperature for 10 minutes. Experiments were performed in duplicates following the instructions from the Arima Hi-C kit (Arima Genomics, San Diego,

CA). Subsequently, Illumina-compatible sequencing libraries were prepared by using a modified version of the KAPA HyperPrep library kit (KAPA BioSystems, Willmington, MA). Quality check steps were performed to assess the fraction of proximally ligated DNA labeled with biotin, and the optimal number of PCR reactions needed to make libraries. The libraries were loaded into an Illumina flowcell (Illumina, San Diego, CA) on a NovaSeq 6000 instrument for paired-end 50 reads.

Hi-C analysis was performed using the HiC-Bench pipeline (Lazaris et al., 2017; Tsirigos et al., 2012) (https://github.com/NYU-BFX/hic-bench). The read pairs were aligned and filtered with the following parameters: Genome-build=mm10; –very-sensitive-local –local; mapq=20; –min-dist 25000 –max-offset 500. The Juicer "pre" tool (Durand et al., 2016) (https:-//github.com/aidenlab/juicer) was used to generate the .hic file with default parameters. Sample duplicates were combined. The compartment analysis was done using the HOMER tool (Heinz et al., 2010) (http://homer.ucsd.edu/homer/index.html) with 100 kb bins. H3K27ac ChIP-seq data was used to assign A/B compartments. Eigenvector-1 bins were considered shifted (AB and BA) when the bin sign changed and the delta value was greater than 1.5. Topologically associated domains (TAD) and boundaries were identified with the HiCRatio method with the follow parameters: –min-lambda=0.0 –max-lambda=1.0 –n-lambda=6 –gamma=0 –distance=500kb –fdr=0.1. The .hic files were converted to .cool format for visualization and plotting with pyGenomeTracks (Lopez-Delisle et al., 2020) at 5 kb resolution.

Loop analysis and RNA-seq integration. The loops were classified into group-specific loops and common loops by using the significance cutoffs provided by Fit-HiC (Ay et al., 2014). A qvalue cutoff of 0.01 was used to identify significant loops in both groups. A loop is considered

"group-specific" if it is only present in one group with a qval < 0.01 and not present in the other group with cutoff of qval < 0.1. Loop anchors were annotated with the gene promoter information (promoter defined as +/– 2 kb from the transcription start site). The genes were classified into "down" and "up" regulated genes using an FDR cutoff of 0.05, logFC cutoff of +/-0.58 and logCPM > 0. "stable" or less changed genes are defined as logFC < 0.38, and logCPM > 0. Random 1,000 genes were chosen for analysis and plotting. The genes were also grouped in "high", "mid" and "low" expression groups by separating the genes in three quantiles according to the logCPM values. For the loop enrichment scores, normalized contact scores were computed using Fit-HiC at 10 kb resolution and bias corrected. Pileup analysis was performed with coolpup.py (Flyamer et al., 2020) with the KR method to balance the weight and random shift controls for distance normalization at 5 kb.

QUANTIFICATION AND STATISTICAL ANALYSIS

Statistical analysis was conducted in GraphPad Prism or R-studio. Specific statistical methods and approaches are indicated for each figure in the figure legend.

Figure legends

Figure 1. *Stag2* ablation in the mouse nervous system causes growth retardation and neurological defects.

(A) PCR analysis of genomic DNA extracted from brains (BR) or livers (LV) of indicated mice.

(B) Immunoblots of brain lysates of *Stag2*$^{f/y}$ and *Stag2*$^{f/y}$*;Cre* mice.

(C) Representative images of *Stag2*$^{f/y}$ and *Stag2*$^{f/y}$*;Cre* mice. Scale bar = 2 cm.

(D) Body weight of *Stag2*$^{f/y}$ and *Stag2*$^{f/y}$*;Cre* mice at different age. Mean ± SD of at least three mice of the same age.

(E) Survival curves of *Stag2*$^{f/y}$ (n = 12) and *Stag2*$^{f/y}$*;Cre* (n = 21) mice.

(F,G) Food (F) and water (G) consumption of 7- to 8-week-old *Stag2*$^{f/y}$ (n = 6) and *Stag2*$^{f/y}$*;Cre* (n = 4) mice. Mean ± SD; ns, not significant.

(H) Plasma IGF-1 levels of two-month-old *Stag2*$^{f/y}$ (n = 5) and *Stag2*$^{f/y}$*;Cre* (n = 6) mice. Mean ± SD; ****$p < 0.0001$

(I) Representative images of limb-clasping responses of *Stag2*$^{f/y}$ and *Stag2*$^{f/y}$*;Cre* mice.

Figure 2. *Stag2* ablation in mouse brains downregulates the expression of myelin genes.

(A) Volcano plot of bulk RNA sequencing results of *Stag2*$^{f/y}$ and *Stag2*$^{f/y}$*;Cre* brain extracts. Top differentially expressed genes (DEGs) are colored blue and labeled. n = 4 pairs of P21 *Stag2*$^{f/y}$ and *Stag2*$^{f/y}$*;Cre* brain hemispheres were used for the comparison.

(B) RT-qPCR analysis of the top downregulated genes in the brain extracts. n = 4 pairs of *Stag2*$^{f/y}$ and *Stag2*$^{f/y}$*;Cre* littermates were used. Mean ± SD.

(C) Heatmap of the expression of myelin-enriched genes that were down-regulated by more than two folds in *Stag2*$^{f/y}$*;Cre* brains. *L1* and *R1*, left and right brain hemispheres of the *Stag2*$^{f/y}$*#1*

mouse. *L2* and *R2*, left and right brain hemispheres of the *Stag2*$^{f/y}$*#2* mouse. *L1'* and *R1'*, left and right brain hemispheres of the *Stag2*$^{f/y}$*;Cre #1* mouse. *L2'* and *R2'*, left and right brain hemispheres of the *Stag2*$^{f/y}$*;Cre#2* mouse. The biological pathways of these genes are labeled on the right.

(D) Top canonical pathways identified by ingenuity pathway analysis (IPA) of the DEGs.

Figure 3. *Stag2* ablation in the nervous system compromises myelination during early postnatal development.

(A) Luxol fast blue staining of the sagittal sections of *Stag2*$^{f/y}$ and *Stag2*$^{f/y}$*;Cre* brains. n = 3 animals per genotype. Scale bar = 1 mm.

(B) Immunohistochemistry staining with the anti-MBP antibody in the cerebral cortex (left panel). Antibody-stained areas and DAPI staining regions are marked with red and yellow dashed lines, respectively. Scale bar = 200 μm. Quantification of the percentage of the myelinated cortex is shown in the right panel. n = 4 pairs of *Stag2*$^{f/y}$ and *Stag2*$^{f/y}$*;Cre* littermates were used (P18 or P21) for the comparison. $^{**}p < 0.01$; Mean ± SD.

(C) Immunohistochemistry staining with the anti-PLP1 antibody in the cerebellum (left panel). Antibody-stained areas and DAPI staining regions are marked with red and yellow dashed lines, respectively. Scale bar = 200 μm. Quantification of the percentage of the myelinated cerebellum granular layer is shown in the right panel. n = 3 pairs of *Stag2*$^{f/y}$ and *Stag2*$^{f/y}$*;Cre* littermates were used (P20 or P25) for the comparison. $^{*}p < 0.05$; Mean ± SD.

(D) Higher magnification images (left panel) of the immunohistochemistry staining with the anti-MBP antibody in (B). Images processed through axial thinning are shown in the right panel. Scale bar = 50 μm.

(E,F) Total fiber length (E) and fiber coherency (F) measured using the processed images in (D). n = 4 pairs of *Stag2*$^{f/y}$ and *Stag2*$^{f/y}$*;Cre* littermates were used (P18 or P21). *p < 0.05, **p < 0.01; Mean ± SD.

(G) Transmission electron microscopy images of the optic nerves (left panel). Scale bar = 2 μm. Quantification of myelinated axon distributions is shown in the right panel. n = 4 pairs of P18 *Stag2*$^{f/y}$ and *Stag2*$^{f/y}$*;Cre* littermates were used. n ≥ 10 fields of each mouse were taken, and the average distribution of myelinated axons were calculated for each mouse and plotted. **p < 0.01; Mean ± SD.

Figure 4. Deletion of *Stag2* in mouse brains causes differentiation delay and transcriptional changes in oligodendrocytes.

(A) *t*-SNE plot of cell clusters in *Stag2*$^{f/y}$ and *Stag2*$^{f/y}$*;Cre* forebrains analyzed by single-cell RNA-seq (scRNA-seq). n = 2 mice of each genotype were used in the scRNA-seq analysis. aNSCs/NPCs, active neural stem cells or neural progenitor cells; Astrocytes/qNSCs, astrocytes or quiescent neural stem cells; OPCcycs, cycling oligodendrocyte (OL) progenitor cells; OPCs, OL progenitor cells; NFOLs, newly formed OLs; mFOLs, myelin-forming OLs; MOLs, matured OLs; VLMCs, vascular and leptomeningeal cells; vSMCs, vascular smooth muscle cells.

(B) *t*-SNE clustering as in (A) but colored by genotype.

(C) Left panel: cell type composition and percentage as colored in (A). Right panel: percentage of cell clusters of the oligodendrocyte lineage.

(D) FeaturePlot of a representative gene (*Mal*) specifically suppressed in MOLs of *Stag2*$^{f/y}$*;Cre* forebrains. A maximum cutoff of 3 was used.

(E) Experimental scheme of the magnetic-activated cell sorting (MACS) of primary OLs.

(F) Volcano plot of bulk RNA-seq results of *Stag2*$^{f/y}$ and *Stag2*$^{f/y}$*;Cre* primary OLs.

(G) Top canonical pathways identified by IPA of the DEGs in (F).

(H) Commons DEGs shared between bulk RNA-seq analyses of the whole brains (WB) and primary OLs.

Figure 5. Loss of *Stag2* does not alter compartments and TADs in oligodendrocytes.

(A) Representative snapshots of balanced Hi-C contact matrices of chromosome 2. Tracks of eigenvector-1 fixed with housekeeping genes are shown below, with A and B compartments shown in red and blue, respectively.

(B) Hexbin plot of eigenvector-1 for genomic bins (100 kb) in *Stag2*$^{f/y}$ and *Stag2*$^{f/y}$*;Cre* oligodendrocytes (OLs).

(C) Chromatin bins were classified into four categories based on the eigenvector sign and whether it has switched with a delta bigger than 1.5. AB, changing from compartment A in *Stag2*$^{f/y}$ to compartment B in *Stag2*$^{f/y}$*;Cre*; BA, from B in *Stag2*$^{f/y}$ to A in *Stag2*$^{f/y}$*;Cre*; AA, A in both *Stag2*$^{f/y}$ and *Stag2*$^{f/y}$*;Cre*; BB, B in both *Stag2*$^{f/y}$ and *Stag2*$^{f/y}$*;Cre*.

(D) Boxplot of averaged gene expression change of DEGs (RNA logFC cutoff of ± 0.58) inside each genomic bin. Bins counted: AA, 1646; AB, 56; BA, 69; BB, 910. Red dots represent the mean value. An unpaired Wilcoxon test was used for the statistical analysis. *$p < 0.05$; **$p < 0.01$; ***$p < 0.001$; ns, not significant.

(E) Principal component analysis (PCA) plot of the insulation score.

(F) Overlaps of TAD boundaries between genotypes and biological replicates.

(G) Pile-up analysis of TAD boundary-centered local structure flanked by 400 kb chromatin regions.

(H) Pile-up analysis of TAD local structure rescaled to an equal size.

Figure 6. *Stag2* deletion impairs the formation of total and promoter-anchored loops in oligodendrocytes.

(A) Loop counts (left panel) and length (right panel) in the indicated categories of *Stag2*$^{f/y}$ and *Stag2*$^{f/y}$*;Cre* oligodendrocytes (OLs).

(B) Loop counts plotted against loop length (from 0 to 5 Mb) of *Stag2*$^{f/y}$ and *Stag2*$^{f/y}$*;Cre* OLs.

(C) Normalized contact counts for loops across different genomic distances in *Stag2*$^{f/y}$ and *Stag2*$^{f/y}$*;Cre* OLs.

(D) Representative snapshots of contact maps at the *Pls1* gene locus. Tracks and narrow peaks from STAG2 and H3K27ac ChIP-seq as well as the loops are plotted below. Transcription direction is indicated by the black arrow.

(E) Pile-up analysis of loop "dots"-centered local maps for the promoter-anchored loops of genes in the indicated categories. The maps are balanced, normalized by distance, and plotted at 5 kb resolution. The numbers indicate the enrichment of the central pixel over the upper left and bottom right corners.

(F) Pile-up analysis of the local contact maps centered around the transcription start site (TSS) of genes in the indicated categories. Transcription directions are indicated below. 1,000 stable genes are chosen randomly and used for the analysis. The maps are balanced, normalized by distance, and plotted at 5kb resolution. Diagonal pixels are omitted.

Figure 7. Proposed roles of STAG2-cohesin-mediated loop extrusion during transcription in oligodendrocytes.

(A) STAG2-cohesin-mediated chromosome looping connects the enhancer and the promoter, thus facilitating interactions among oligodendrocyte-specific transcription factors, the mediator complex, and the general transcription machinery including RNA polymerase II.

(B) STAG2-cohesin travels along the gene body via transcription-coupled loop extrusion to facilitate pre-mRNA processing.

(C) STAG2-cohesin mediates the formation of gene loops that bring the terminator close to the promoter and facilitate Pol II recycling for multiple rounds of transcription.

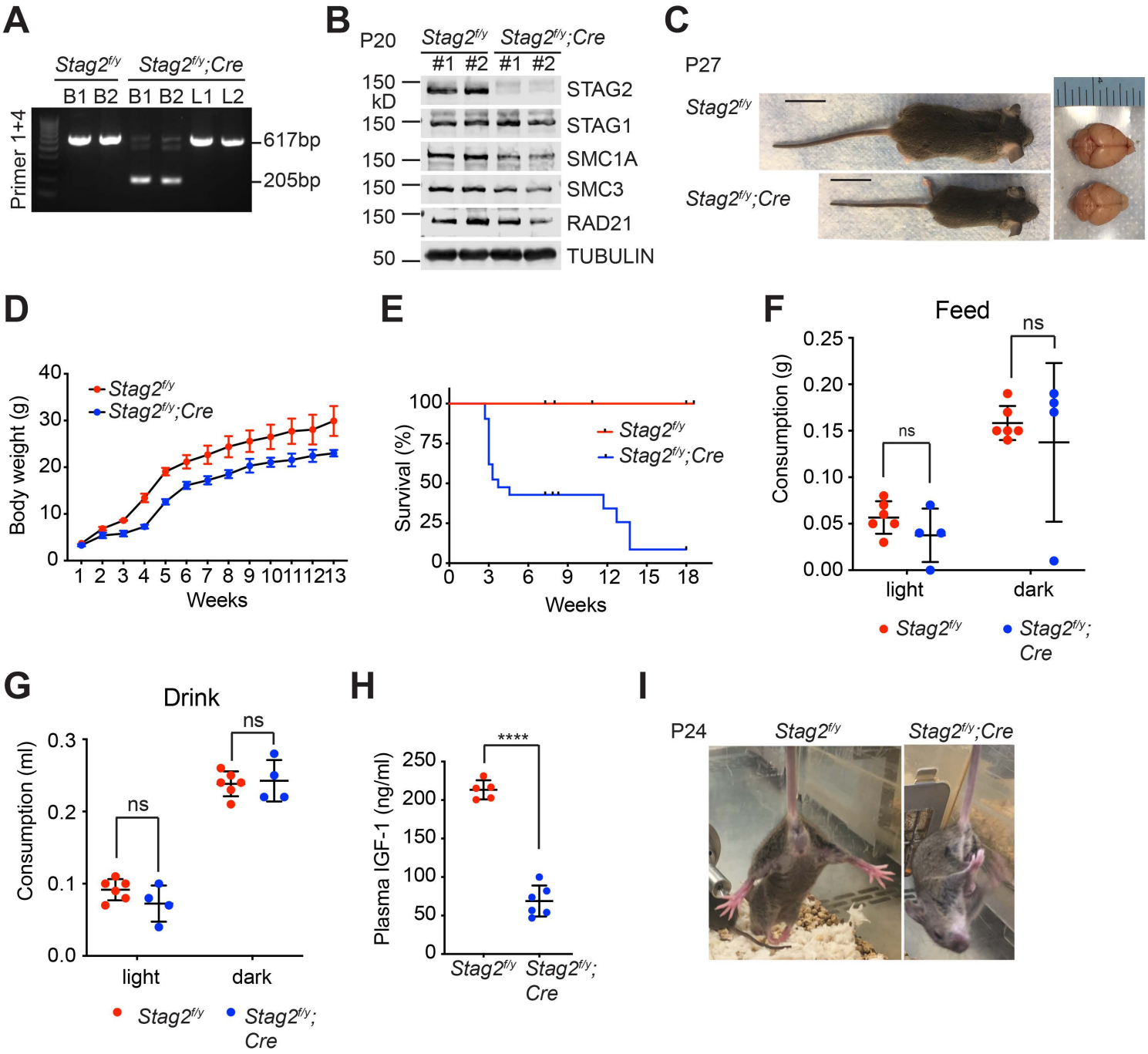
A
Stag2f/y
Stag2f/y;Cre
B1 B2 B1 B2 L1 L2
Primer 1+4
617bp
205bp
B
P20
Stag2f/y
Stag2f/y;Cre
#1 #2 #1 #2
150 kD
STAG2
STAG1
SMC1A
SMC3
RAD21
TUBULIN
50
C
P27
Stag2f/y
Stag2f/y;Cre
D
Body weight (g)
Weeks
Stag2f/y
Stag2f/y;Cre
E
Survival (%)
Weeks
Stag2f/y
Stag2f/y;Cre
F
Feed
Consumption (g)
ns
ns
light
dark
Stag2f/y
Stag2f/y; Cre
G
Drink
Consumption (ml)
ns
ns
light
dark
Stag2f/y
Stag2f/y; Cre
H
Plasma IGF-1 (ng/ml)
****
Stag2f/y
Stag2f/y; Cre
I
P24
Stag2f/y
Stag2f/y;Cre

Figure 1

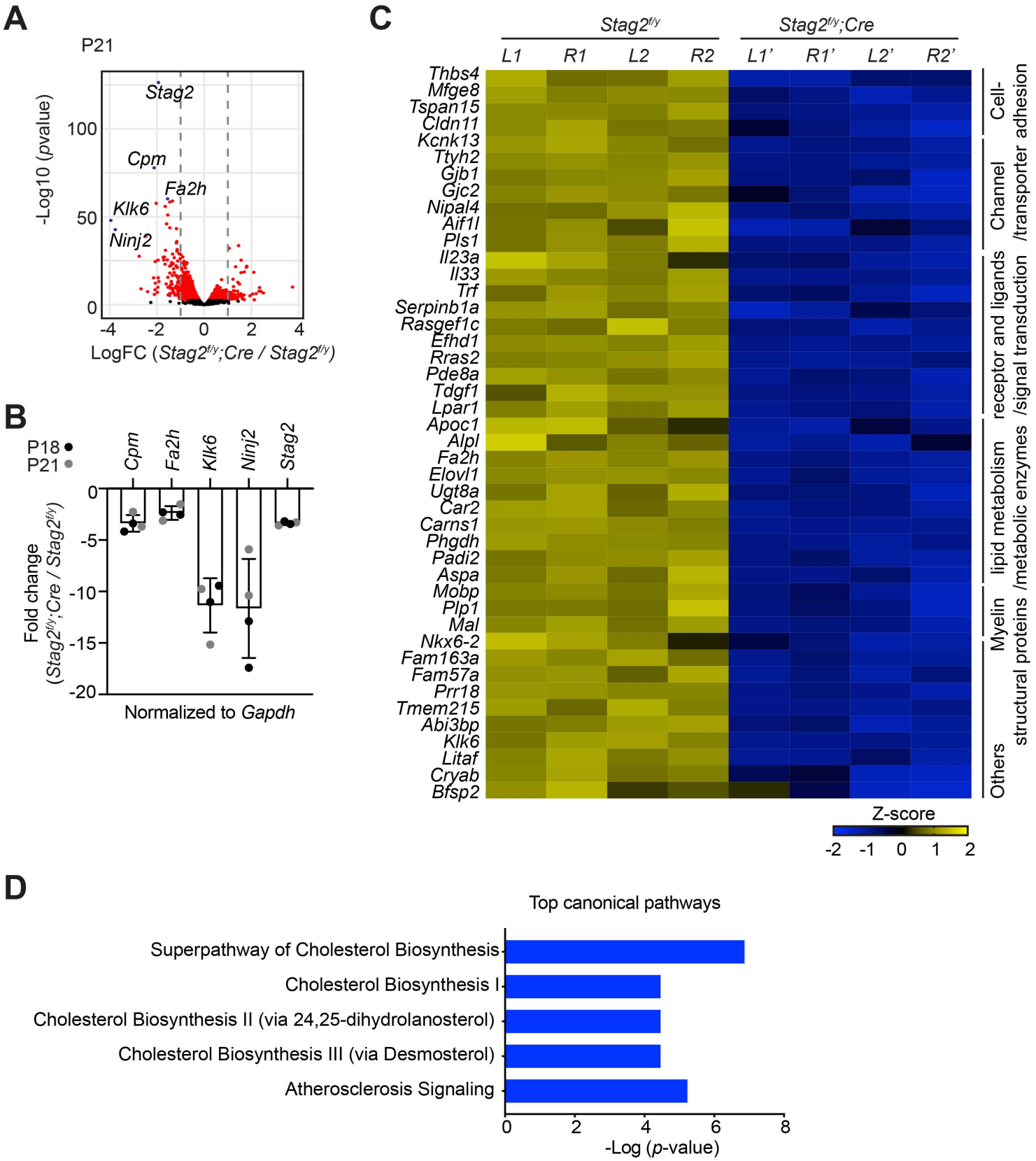
A
P21
Stag2
Cpm
Fa2h
Klk6
Ninj2
-Log10 (pvalue)
LogFC (Stag2f/y;Cre / Stag2f/y)
B
P18
P21
Cpm
Fa2h
Klk6
Ninj2
Stag2
Fold change (Stag2f/y;Cre / Stag2f/y)
Normalized to Gapdh
C
Stag2f/y
Stag2f/y;Cre
L1
R1
L2
R2
L1'
R1'
L2'
R2'
Thbs4
Mfge8
Tspan15
Cldn11
Kcnk13
Ttyh2
Gjb1
Gjc2
Nipal4
Aif1l
Pls1
Il23a
Il33
Trf
Serpinb1a
Rasgef1c
Efhd1
Rras2
Pde8a
Tdgf1
Lpar1
Apoc1
Alpl
Fa2h
Elovl1
Ugt8a
Car2
Carns1
Phgdh
Padi2
Aspa
Mobp
Plp1
Mal
Nkx6-2
Fam163a
Fam57a
Prr18
Tmem215
Abi3bp
Klk6
Litaf
Cryab
Bfsp2
Cell-adhesion
Channel /transporter
receptor and ligands /signal transduction
lipid metabolism /metabolic enzymes
Myelin structural proteins
Others
Z-score
D
Top canonical pathways
Superpathway of Cholesterol Biosynthesis
Cholesterol Biosynthesis I
Cholesterol Biosynthesis II (via 24,25-dihydrolanosterol)
Cholesterol Biosynthesis III (via Desmosterol)
Atherosclerosis Signaling
-Log (p-value)

Figure 2

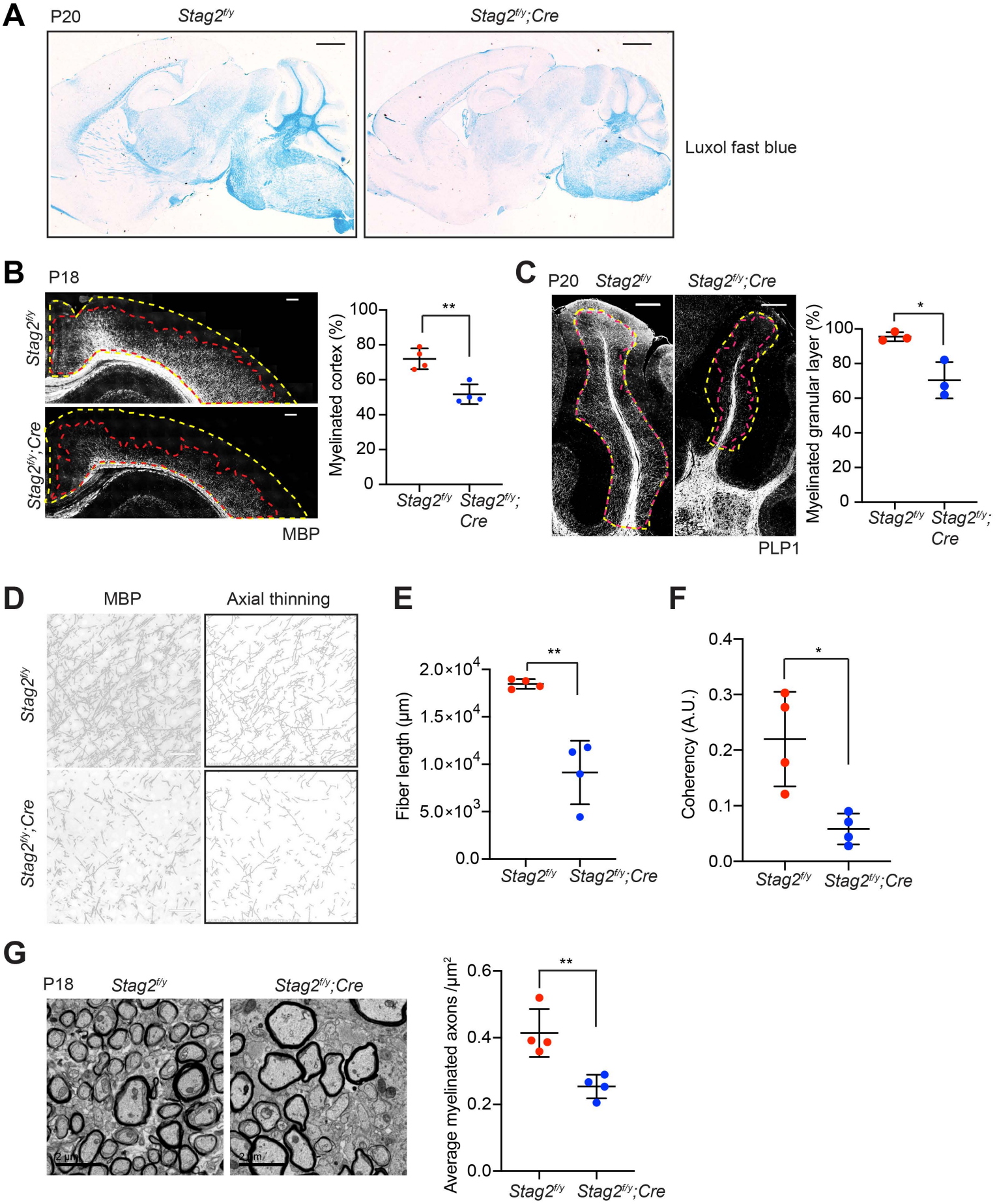
A
P20
Stag2f/y
Stag2f/y;Cre
Luxol fast blue
B
P18
Stag2f/y
Stag2f/y;Cre
MBP
Myelinated cortex (%)
100
80
60
40
20
0
**
Stag2f/y
Stag2f/y; Cre
C
P20
Stag2f/y
Stag2f/y;Cre
PLP1
Myelinated granular layer (%)
100
80
60
40
20
0
*
Stag2f/y
Stag2f/y; Cre
D
MBP
Axial thinning
Stag2f/y
Stag2f/y;Cre
E
Fiber length (μm)
2.0×10^4
1.5×10^4
1.0×10^4
5.0×10^3
0.0
**
Stag2f/y
Stag2f/y;Cre
F
Coherency (A.U.)
0.4
0.3
0.2
0.1
0.0
*
Stag2f/y
Stag2f/y;Cre
G
P18
Stag2f/y
Stag2f/y;Cre
2 μm
2 μm
Average myelinated axons /μm2
0.6
0.4
0.2
0.0
**
Stag2f/y
Stag2f/y;Cre

Figure 3

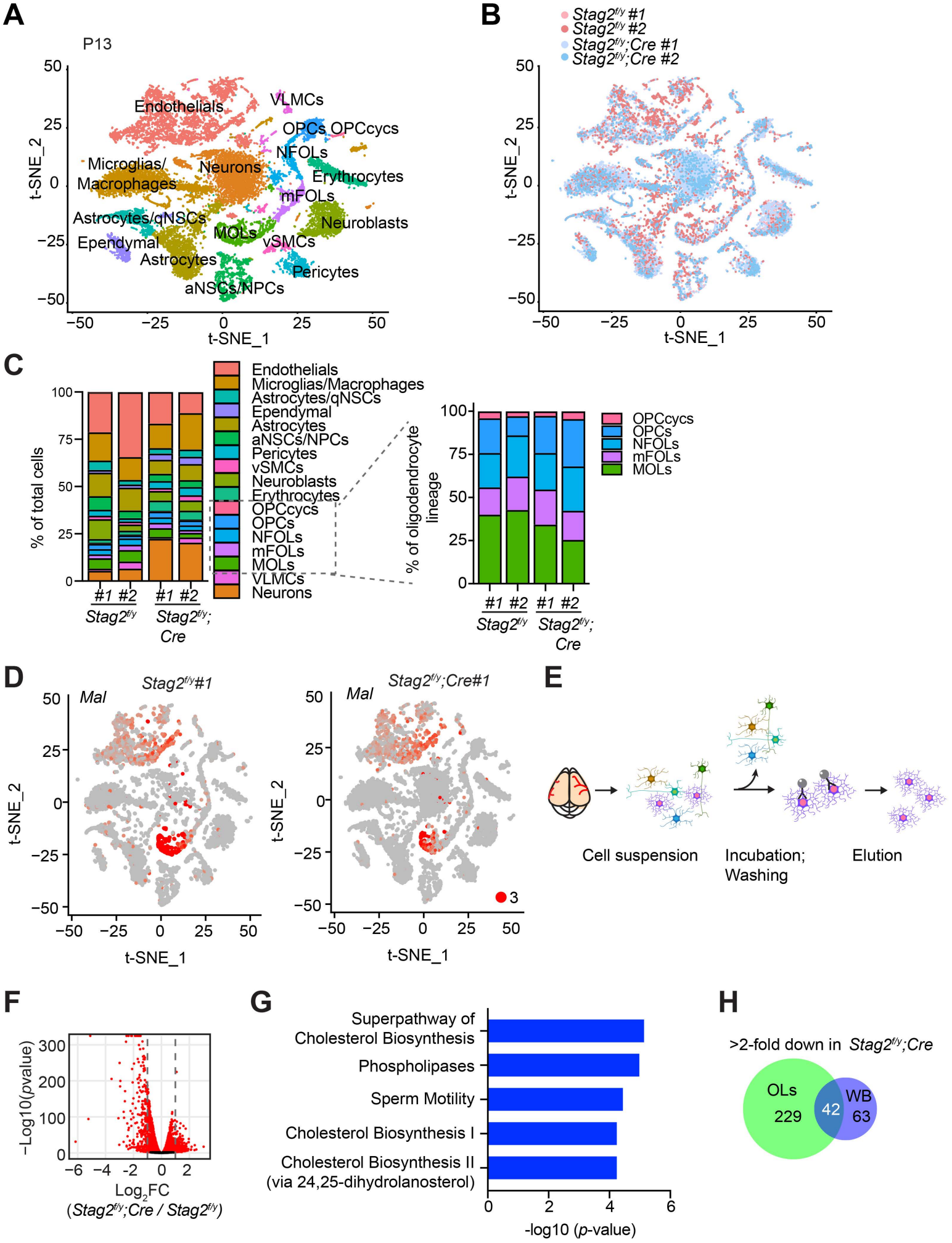
A
P13
Endothelials
VLMCs
OPCs OPCcycs
NFOLs
Microglias/
Macrophages
Neurons
Erythrocytes
mFOLs
Astrocytes/qNSCs
Neuroblasts
MOLs
vSMCs
Ependymal
Astrocytes
Pericytes
aNSCs/NPCs
t-SNE_1
t-SNE_2
B
Stag2f/y #1
Stag2f/y #2
Stag2f/y;Cre #1
Stag2f/y;Cre #2
C
% of total cells
% of oligodendrocyte lineage
OPCcycs
OPCs
NFOLs
mFOLs
MOLs
VLMCs
Neurons
#1 #2 #1 #2
Stag2f/y
Stag2f/y; Cre
D
Stag2f/y#1
Stag2f/y;Cre#1
Mal
3
E
Cell suspension
Incubation; Washing
Elution
F
−Log10(pvalue)
Log2FC
(Stag2f/y;Cre / Stag2f/y)
G
Superpathway of Cholesterol Biosynthesis
Phospholipases
Sperm Motility
Cholesterol Biosynthesis I
Cholesterol Biosynthesis II (via 24,25-dihydrolanosterol)
-log10 (p-value)
H
>2-fold down in Stag2f/y;Cre
OLs
229
42
WB
63

Figure 4

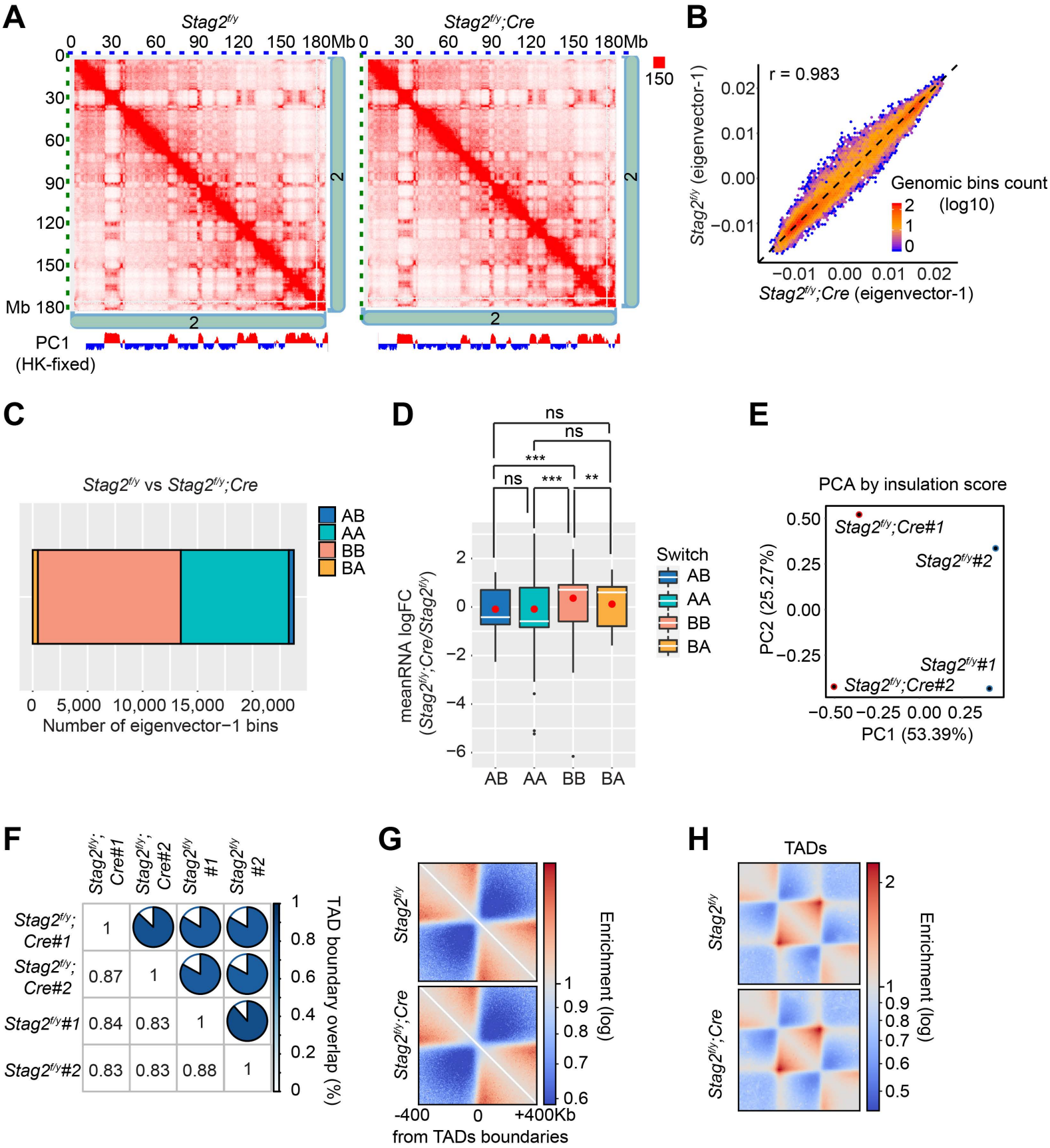
A
Stag2f/y
Stag2f/y;Cre
0 30 60 90 120 150 180Mb
150
Mb 180
PC1
(HK-fixed)
B
r = 0.983
Stag2f/y (eigenvector-1)
Stag2f/y;Cre (eigenvector-1)
Genomic bins count
(log10)
C
Stag2f/y vs Stag2f/y;Cre
AB
AA
BB
BA
Number of eigenvector−1 bins
D
meanRNA logFC
(Stag2f/y;Cre/Stag2f/y)
Switch
ns
***
**
E
PCA by insulation score
Stag2f/y;Cre#1
Stag2f/y#2
Stag2f/y#1
Stag2f/y;Cre#2
PC2 (25.27%)
PC1 (53.39%)
F
TAD boundary overlap (%)
G
Enrichment (log)
-400 0 +400Kb
from TADs boundaries
H
TADs

Figure 5

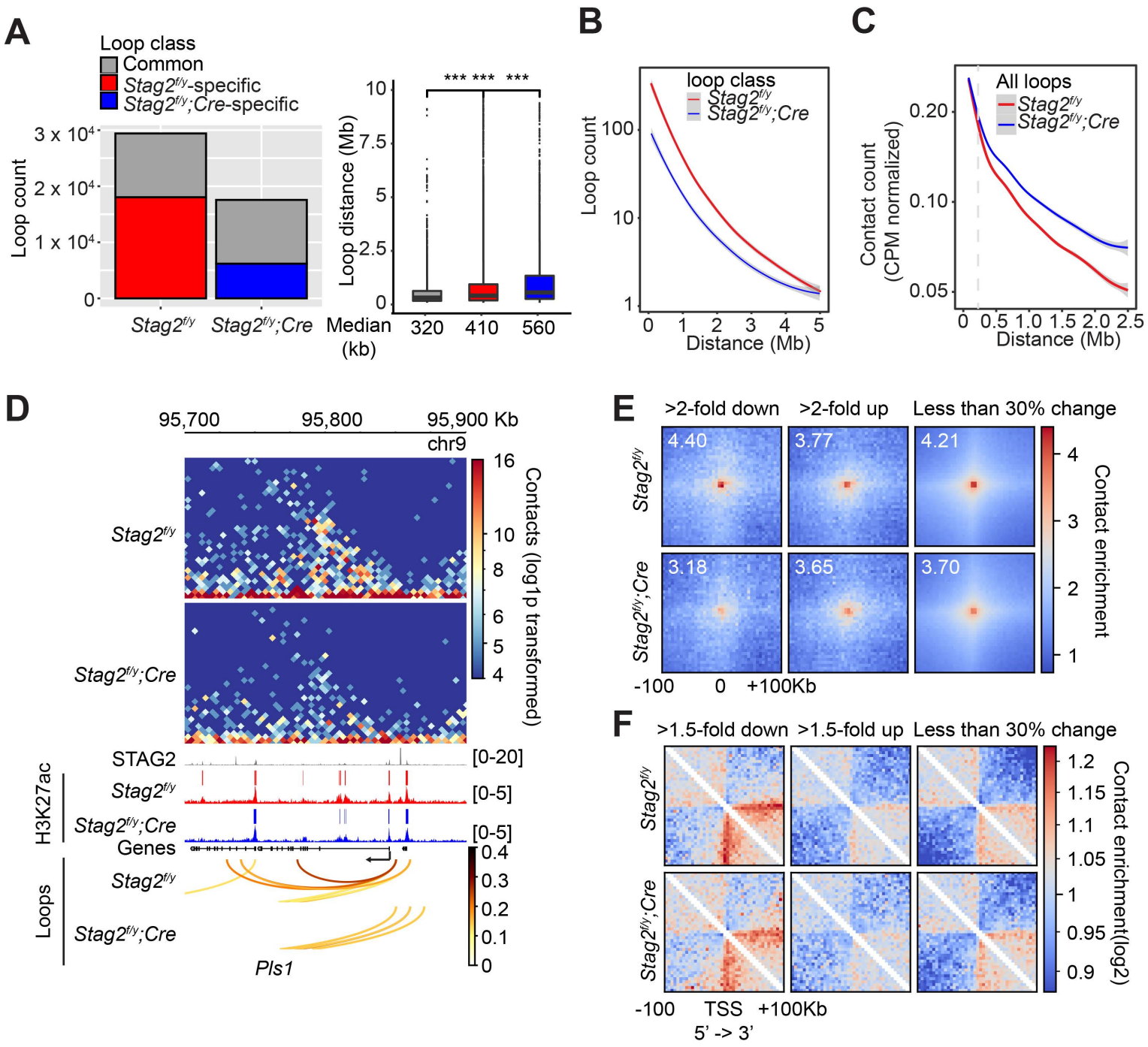
A
Loop class
Common
Stag2f/y-specific
Stag2f/y;Cre-specific
Loop count
3 x 10^4
2 x 10^4
1 x 10^4
0
Stag2f/y
Stag2f/y;Cre
Loop distance (Mb)
10
7.5
5
2.5
0
*** *** ***
Median (kb)
320
410
560
B
loop class
Stag2f/y
Stag2f/y;Cre
Loop count
100
10
1
0 1 2 3 4 5
Distance (Mb)
C
All loops
Stag2f/y
Stag2f/y;Cre
Contact count (CPM normalized)
0.20
0.10
0.05
0 0.5 1.0 1.5 2.0 2.5
Distance (Mb)
D
95,700
95,800
95,900 Kb
chr9
Stag2f/y
Stag2f/y;Cre
Contacts (log1p transformed)
16
10
8
6
5
4
STAG2
[0-20]
H3K27ac
Stag2f/y
[0-5]
Stag2f/y;Cre
[0-5]
Genes
Loops
Stag2f/y
Stag2f/y;Cre
0.4
0.3
0.2
0.1
0
Pls1
E
>2-fold down
>2-fold up
Less than 30% change
Stag2f/y
Stag2f/y;Cre
4.40
3.77
4.21
3.18
3.65
3.70
Contact enrichment
4
3
2
1
-100
0
+100Kb
F
>1.5-fold down
>1.5-fold up
Less than 30% change
Stag2f/y
Stag2f/y;Cre
Contact enrichment(log2)
1.2
1.15
1.1
1.05
1
0.95
0.9
-100
TSS
+100Kb
5' -> 3'

Figure 6

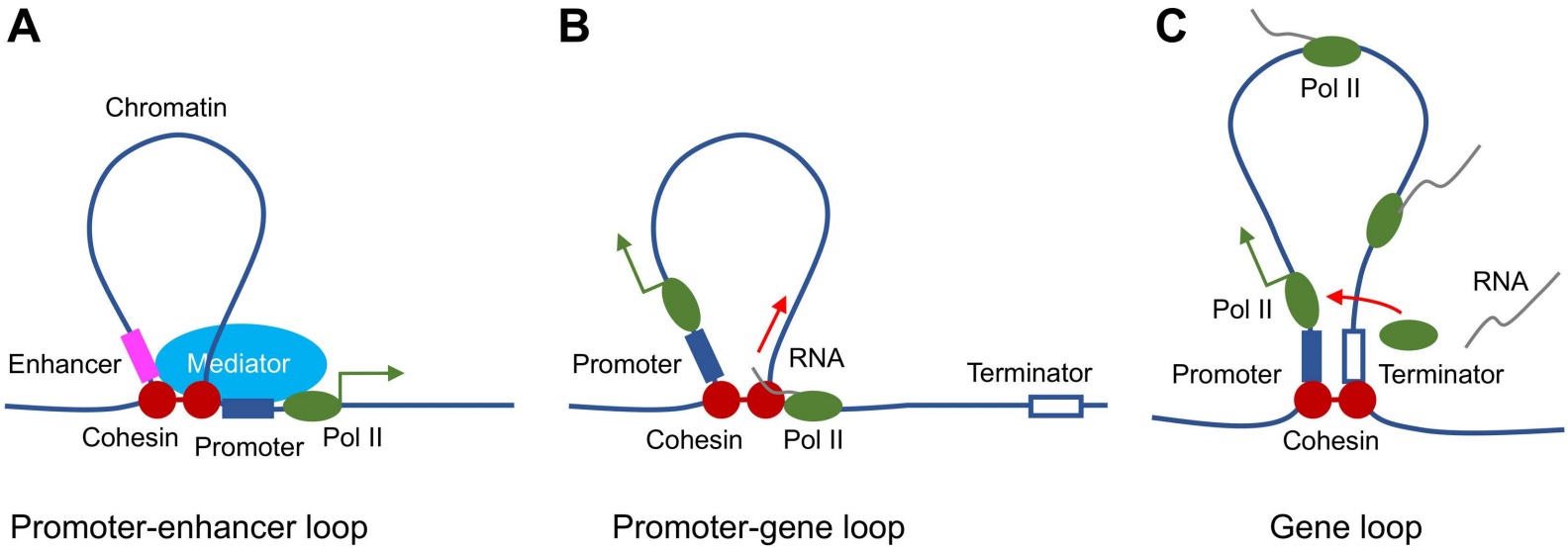
A
Chromatin
Enhancer
Mediator
Cohesin
Promoter
Pol II
Promoter-enhancer loop
B
Promoter
RNA
Terminator
Cohesin
Pol II
Promoter-gene loop
C
Pol II
Pol II
RNA
Promoter
Terminator
Cohesin
Gene loop

Figure 7

KEY RESOURCES TABLE

REAGENT or RESOURCE	SOURCE	IDENTIFIER
Antibodies		
Rabbit anti-STAG2	In-house	N/A
Mouse anti-α-TUBULIN	Sigma-Aldrich	T9026, RRID:AB_477593
Rabbit anti-STAG1	Bethyl Laboratories	A302-579A, RRID:AB_2034857
Rabbit anti-SMC1A	Bethyl Laboratories	A300-055A, RRID:AB_2192467
Rabbit anti-SMC3	Bethyl Laboratories	A300-060A, RRID:AB_67579
Rabbit anti-RAD21	Bethyl Laboratories	A300-080a, RRID:AB_2176615
Rat anti-MBP	Abcam	ab7349, RRID:AB_305869
Rabbit anti-PLP1	Abcam	ab28486, RRID:AB_776593
Rabbit anti-H3K27ac	Abcam	ab4729, RRID:AB_2118291
Mouse anti-O4 MicroBeads	Miltenyi Biotec	130-094-543, RRID:AB_2847907
Goat anti-rabbit IgG (H+L) (DyLight 800 Conjugate)	Cell Signaling Technology	5151S, RRID:AB_10697505
Goat anti-mouse IgG (H+L) (DyLight 680 Conjugate)	Cell Signaling Technology	5470S, AB_10696895
Goat anti-rat IgG (H+L) Alexa Fluor 568	Thermo Fisher Scientific	A-11077, RRID:AB_2534121
Goat anti-rabbit IgG (H+L) Alexa Fluor 488	Thermo Fisher Scientific	A-11008, RRID:AB_143165
Chemicals, peptides, and recombinant proteins		
Papain	Worthington Biochemical	LS003119
Deoxyribonuclease I	Worthington Biochemical	LS002007
Insulin	Sigma-Aldrich	I6634
Biotin	Sigma-Aldrich	B4639
L-Glutamine	Gibco	25030-164
N-Acetyl-L-cysteine	Sigma-Aldrich	A8199
Forskolin	Sigma-Aldrich	F6886
CNTF	PeproTECH	450-13
PDGF-AA	PeproTECH	100-13A
NT-3	PeproTECH	450-03
Sarkosyl	Sigma-Aldrich	L7414
Apo-transferrin	Sigma-Aldrich	T1147
Putrescine	Sigma-Aldrich	P5780
Progesterone	Sigma-Aldrich	P8783
Sodium selenite	Sigma-Aldrich	S5261
DAPI	Sigma-Aldrich	D9564
Xylenes	Fisher Scientific	X3S-4
Paraformaldehyde	Sigma-Aldrich	158127

Tamoxifen	Sigma-Aldrich	T5648
(Z)-4-Hydroxytamoxifen	Sigma-Aldrich	H7904
UTPαS, [35S]	Perkin Elmer	NEG039H
Critical commercial assays		
DNeasy Blood & Tissue Kit	Qiagen	69506
Precellys lysing kit (Soft tissue homogenizing)	Bertin Instruments	P000912-LYSK0-A.0
Mouse/rat IGF1 Quantikine ELISA kit	R&D systems	MG100
Rat/Mouse Growth Hormone ELISA kit	EMD Millipore	EZRMGH-45K
PCR Purification Kit	Qiagen	28106
Papain Dissociation System	Worthington Biochemical	LK003150
TruSeq Stranded mRNA Library Prep kit	Illlumina	20020594
High-Capacity cDNA Reverse Transcription kit	Applied Biosystems	4368814
TaqMan Gene Expression Master Mix	Applied Biosystems	4369016
Chromium Single Cell 3' GEM, Library & Gel Bead Kit v3	10x Genomics	1000092
KAPA HyperPrep Kits	Kapa Biosystems	KK8503
Next Gen DNA Library Kit	Active Motif	53216
Next Gen Indexing Kit	Active Motif	53264
Arima-HiC Kit	Arima Genomics	510008
Deposited data		
RNA-seq, scRNA-seq, ChIP-seq and Hi-C data	This study	GEOXXX
Experimental models: Organisms/strains		
Mouse: *Stag2 -/+*	This study	N/A
Mouse: *Stag2 flox/flox*	This study	N/A
Mouse: FVB/NJ	The Jackson Laboratory	001800, RRID:IMSR_JAX:001800
Mouse: C57BL/6J	The Jackson Laboratory	000664, RRID:IMSR_JAX:000664
Mouse: B6.129-Gt(ROSA)26Sortm1(cre/ERT2)Tyj/J	The Jackson Laboratory	008463, RRID:IMSR_JAX:008463
Mouse: B6.Cg-Tg(Nes-cre)1Kln/J	The Jackson Laboratory	003771, RRID:IMSR_JAX:003771
Oligonucleotides		
TaqMan Gene Expression Assay: *Stag2*	Thermo Fisher Scientific	Mm01311611_m1
TaqMan Gene Expression Assay: *Klk6*	Thermo Fisher Scientific	Mm00478322_m1
TaqMan Gene Expression Assay: *Ninj2*	Thermo Fisher Scientific	Mm00450216_m1
TaqMan Gene Expression Assay: *Cpm*	Thermo Fisher Scientific	Mm01250802_m1
TaqMan Gene Expression Assay: *Fa2h*	Thermo Fisher Scientific	Mm00626259_m1
TaqMan Gene Expression Assay: *Gapdh*	Thermo Fisher Scientific	Mm99999915_g1
Primers containing sgRNAs target sequences on *Stag2* (Table 1)	Integrated DNA Technologies	N/A

Primers for the *Stag2* flox/flox mice genotyping (Table 1)	Integrated DNA Technologies	N/A
Primers for the constructs for the riboprobe synthesis (Table 1)	Integrated DNA Technologies	N/A
Software and algorithms		
GraphPad Prism	GraphPad Software	RRID:SCR_002798, https://www.graphpad.com/scientific-software/prism/
ImageJ (Fiji)	ImageJ	RRID:SCR_002285, https://imagej.net/software/fiji/
RStudio	The R Foundation	RRID:SCR_000432, https://www.rstudio.com/
Bcl2fastq	Illumina	v2.17, RRID:SCR_015058
Fastqc	(Andrews, 2010)	v0.11.2, RRID:SCR_014583
Fastq_screen	(Wingett, 2011)	v0.4.4, RRID:SCR_000141
STAR	(Dobin et al., 2013)	RRID:SCR_004463, https://github.com/alexdobin/STAR
FeatureCounts	(Liao et al., 2014)	RRID:SCR_012919, https://bioconductor.org/packages/release/bioc/html/Rsubread.html
edgeR	(Robinson et al., 2010)	RRID:SCR_012802, https://bioconductor.org/packages/release/bioc/html/edgeR.html
Ingenuity Pathway Analysis	QIAGEN, (Kramer et al., 2014)	RRID:SCR_008653, https://www.qiagenbioinformatics.com/products/ingenuity-pathway-analysis
Bowtie2	(Langmead and Salzberg, 2012)	v2.2.3, RRID:SCR_016368
Picard MarkDuplicates	Broad Institute, GitHub Repository, http://broadinstitute.github.io/picard/	v1.127 RRID:SCR_006525
MACS2	(Zhang et al., 2008)	v2.0.10, RRID:SCR_013291
HOMER	(Heinz et al., 2010; Ross-Innes et al., 2012)	RRID:SCR_010881, http://homer.ucsd.edu/homer/
Deeptools	(Ramirez et al., 2016)	RRID:SCR_016366, https://deeptools.readthedocs.io/en/develop/

Galaxy	(Afgan et al., 2018)	RRID:SCR_006281, https://usegalaxy.org
Cell Ranger	10x Genomics	RRID:SCR_017344, https://support.10xgenomics.com/single-cell-gene-expression/software/pipelines/latest/using/mkfastq
Seurat	Satija Lab, New York Genome Center, (Stuart et al., 2019)	RRID:SCR_016341, https://satijalab.org/seurat
Monocle3	Cole Trapnell's Lab, UW Genome Sciences, (Cao et al., 2019)	RRID:SCR_018685, https://cole-trapnell-lab.github.io/monocle3/
HiC-Bench pipeline	(Lazaris et al., 2017; Tsirigos et al., 2012)	https://github.com/NYU-BFX/hic-bench
Juicer "pre" tool	Aiden Lab, (Durand et al., 2016)	RRID:SCR_017226, https://github.com/aidenlab/juicer
Juicebox	Aiden Lab, BCM	RRID:SCR_021172, https://github.com/aidenlab/Juicebox
Hic2cool	(Abdennur and Mirny, 2020)	https://github.com/4dn-dcic/hic2cool
pyGenomeTracks	(Lopez-Delisle et al., 2020)	https://github.com/deeptools/pyGenomeTracks
Fit-HiC	(Ay et al., 2014)	https://github.com/ay-lab/fithic
Coolpup.py	(Flyamer et al., 2020)	https://github.com/open2c/coolpuppy
Other		
Precellys Minilys Tissue homogenizer	Bertin Instruments	EQ06404.200.RD000.0
Odyssey Infrared Imaging System	LI-COR	9140
LS Columns	Miltenyi Biotec	130-042-401
MidiMACS separator	Miltenyi Biotec	130-042-302
MACS MultiStand	Miltenyi Biotec	130-042-303
Dynabeads Protein A	Invitrogen	10002D
Phenol:chloroform:isoamyl Alcohol 25:24:1	Sigma-Aldrich	P3803
Chloroform:Isoamyl alcohol 24:1	Sigma-Aldrich	C0549
ProLong Gold Antifade Mountant	Fisher Scientific	P36934
Proteinase K	New England Biolabs	P8107S
RNase A	Qiagen	19101
Neurobasal Medium	Thermo Fisher Scientific	21103049
DMEM	Thermo Fisher Scientific	11965-118
Penicillin-Streptomycin	Thermo Fisher Scientific	15140-163
Ambion TRIzol Reagent	Invitrogen	15-596-018

Complete, EDTA-free Protease Inhibitor Cocktail	Sigma-Aldrich	5056489001
Formaldehyde solution	Sigma-Aldrich	F8775
B-27 Serum-Free Supplement	Thermo Fisher Scientific	17504044
Trace Elements B	Corning	25-022-CI
Sodium Pyruvate	Thermo Fisher Scientific	11360-070
DPBS, calcium, magnesium	Thermo Fisher Scientific	14040182
DPBS, no calcium, no magnesium	Thermo Fisher Scientific	14190144
Bovine Serum Albumin	Sigma-Aldrich	A4161

References

Abdennur, N., and Mirny, L.A. (2020). Cooler: scalable storage for Hi-C data and other genomically labeled arrays. Bioinformatics *36*, 311-316.

Afgan, E., Baker, D., Batut, B., van den Beek, M., Bouvier, D., Cech, M., Chilton, J., Clements, D., Coraor, N., Gruning, B.A.*, et al.* (2018). The Galaxy platform for accessible, reproducible and collaborative biomedical analyses: 2018 update. Nucleic Acids Res *46*, W537-W544.

Andrews, S. (2010). FastQC: a quality control tool for high throughput sequence data.

Ay, F., Bailey, T.L., and Noble, W.S. (2014). Statistical confidence estimation for Hi-C data reveals regulatory chromatin contacts. Genome Res *24*, 999-1011.

Cao, J., Spielmann, M., Qiu, X., Huang, X., Ibrahim, D.M., Hill, A.J., Zhang, F., Mundlos, S., Christiansen, L., Steemers, F.J.*, et al.* (2019). The single-cell transcriptional landscape of mammalian organogenesis. Nature *566*, 496-502.

Dobin, A., Davis, C.A., Schlesinger, F., Drenkow, J., Zaleski, C., Jha, S., Batut, P., Chaisson, M., and Gingeras, T.R. (2013). STAR: ultrafast universal RNA-seq aligner. Bioinformatics *29*, 15-21.

Durand, N.C., Shamim, M.S., Machol, I., Rao, S.S., Huntley, M.H., Lander, E.S., and Aiden, E.L. (2016). Juicer Provides a One-Click System for Analyzing Loop-Resolution Hi-C Experiments. Cell Syst *3*, 95-98.

Flyamer, I.M., Illingworth, R.S., and Bickmore, W.A. (2020). Coolpup.py: versatile pile-up analysis of Hi-C data. Bioinformatics *36*, 2980-2985.

Heinz, S., Benner, C., Spann, N., Bertolino, E., Lin, Y.C., Laslo, P., Cheng, J.X., Murre, C., Singh, H., and Glass, C.K. (2010). Simple combinations of lineage-determining transcription factors prime cis-regulatory elements required for macrophage and B cell identities. Mol Cell *38*, 576-589.

Kramer, A., Green, J., Pollard, J., Jr., and Tugendreich, S. (2014). Causal analysis approaches in Ingenuity Pathway Analysis. Bioinformatics *30*, 523-530.

Langmead, B., and Salzberg, S.L. (2012). Fast gapped-read alignment with Bowtie 2. Nat Methods *9*, 357-359.

Lazaris, C., Kelly, S., Ntziachristos, P., Aifantis, I., and Tsirigos, A. (2017). HiC-bench: comprehensive and reproducible Hi-C data analysis designed for parameter exploration and benchmarking. BMC Genomics *18*, 22.

Liao, Y., Smyth, G.K., and Shi, W. (2014). featureCounts: an efficient general purpose program for assigning sequence reads to genomic features. Bioinformatics *30*, 923-930.

Lopez-Delisle, L., Rabbani, L., Wolff, J., Bhardwaj, V., Backofen, R., Gruning, B., Ramirez, F., and Manke, T. (2020). pyGenomeTracks: reproducible plots for multivariate genomic data sets. Bioinformatics.
Ramirez, F., Ryan, D.P., Gruning, B., Bhardwaj, V., Kilpert, F., Richter, A.S., Heyne, S., Dundar, F., and Manke, T. (2016). deepTools2: a next generation web server for deep-sequencing data analysis. Nucleic Acids Res *44*, W160-165.
Robinson, M.D., McCarthy, D.J., and Smyth, G.K. (2010). edgeR: a Bioconductor package for differential expression analysis of digital gene expression data. Bioinformatics *26*, 139-140.
Ross-Innes, C.S., Stark, R., Teschendorff, A.E., Holmes, K.A., Ali, H.R., Dunning, M.J., Brown, G.D., Gojis, O., Ellis, I.O., Green, A.R*., et al.* (2012). Differential oestrogen receptor binding is associated with clinical outcome in breast cancer. Nature *481*, 389-393.
Stuart, T., Butler, A., Hoffman, P., Hafemeister, C., Papalexi, E., Mauck, W.M., 3rd, Hao, Y., Stoeckius, M., Smibert, P., and Satija, R. (2019). Comprehensive Integration of Single-Cell Data. Cell *177*, 1888-1902 e1821.
Tsirigos, A., Haiminen, N., Bilal, E., and Utro, F. (2012). GenomicTools: a computational platform for developing high-throughput analytics in genomics. Bioinformatics *28*, 282-283.
Wingett, S. (2011). FastQ Screen: quality control tool to screen a library of sequences in FastQ format against a set of sequence databases. .
Zhang, Y., Liu, T., Meyer, C.A., Eeckhoute, J., Johnson, D.S., Bernstein, B.E., Nusbaum, C., Myers, R.M., Brown, M., Li, W*., et al.* (2008). Model-based analysis of ChIP-Seq (MACS). Genome Biol *9*, R137.

Supplemental Information

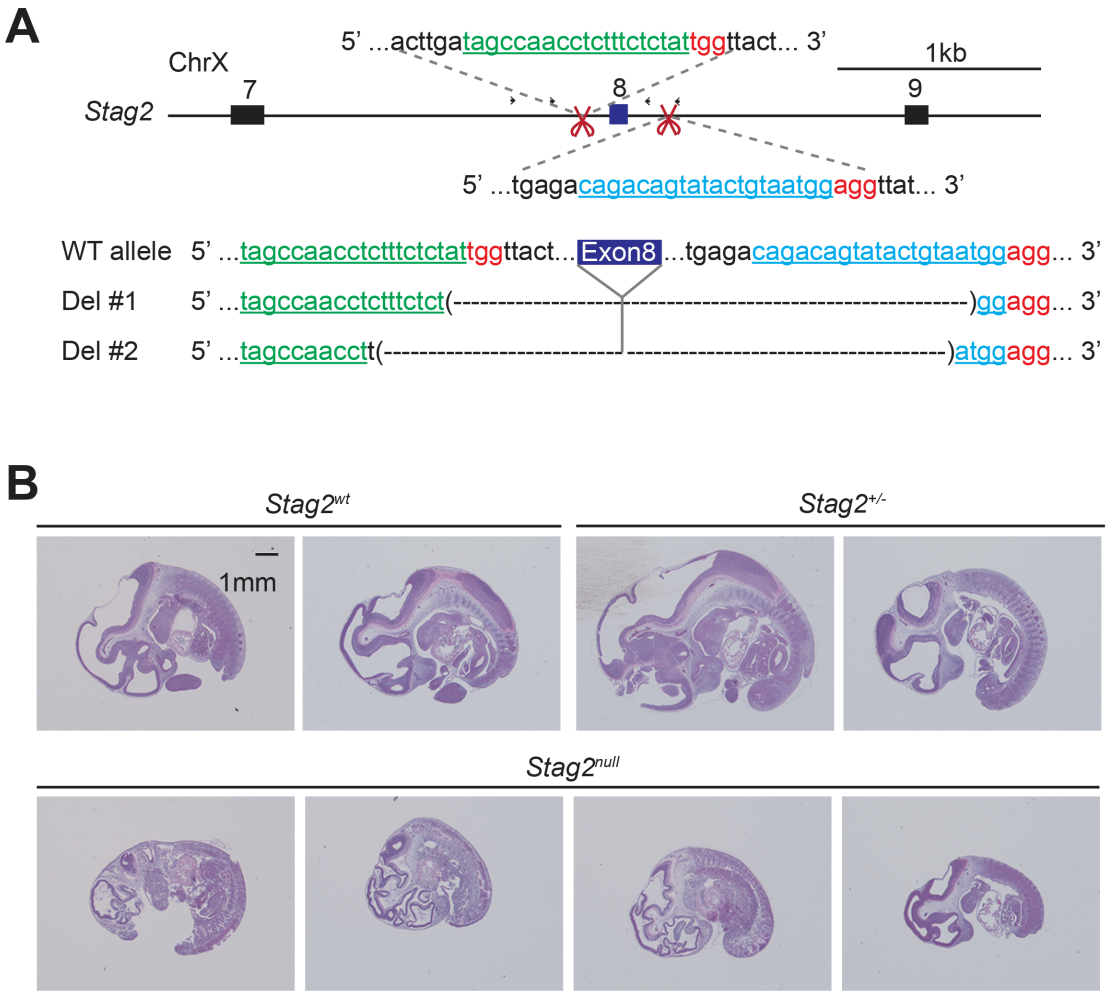

Figure S1. Generation of *Stag2* knockout mice using the CRISPR/Cas9 method.
(A) Scheme for disrupting *Stag2* in the mouse genome using CRISPR/Cas9 with guide RNAs flanking exon 8. Sequencing analysis of the genomic DNA extracted from two *Stag2*-disrupted founder mice is shown below.
(B) Hematoxylin and eosin (H&E) staining of sagittal sections of F2 embryos derived from F1 in (A) at E11.5.

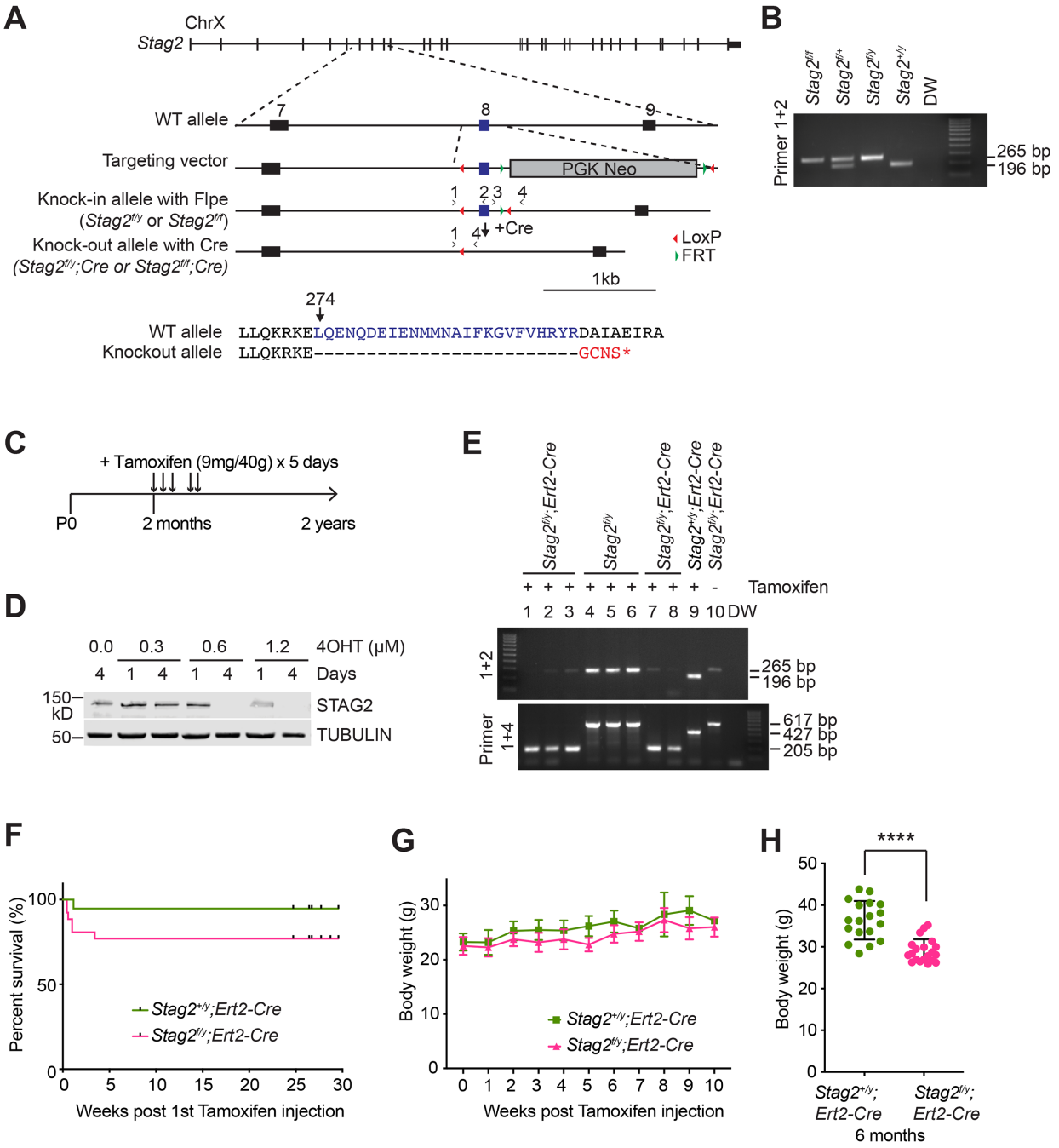

Figure S2. Generation of *Stag2* conditional knockout mice by gene targeting.
(A) Scheme for creating the "floxed" *Stag2* allele by gene targeting. The genomic structure of the wild-type (WT) *Stag2* locus, the targeting vector, the knock-in allele, the disrupted allele after Cre-mediated recombination, and the positions of the genotyping primers are shown. The amino acid sequence of the knockout allele in the targeted region is shown and aligned with that of the WT allele.
(B) PCR analysis of the genomic DNA extracted from the tails of indicated mice with the primers in (A).

(C) Experimental scheme of tamoxifen injection into adult *Stag2*$^{f/y}$*;Ert2-Cre* and *Stag*$^{+/y}$*;Ert2-Cre* mice.
(D) Western blotting of cell extracts from *Stag2*$^{f/y}$*;Ert2-Cre* mouse embryonic fibroblasts (MEF) treated with or without 4-hydroxytamoxifen (4OHT).
(E) PCR analysis of the genomic DNA extracted from the blood of indicated mice with the primers in (A).
(F) Survival curves of *Stag2*$^{f/y}$*;Ert2-Cre* (n=26) and *Stag*$^{+/y}$*;Ert2-Cre* (n=19) mice after tamoxifen injection.
(G) Body weight of mice in (F).
(H) Body weight of *Stag2*$^{f/y}$*;Ert2-Cre* (n=20) and *Stag*$^{+/y}$*;Ert2-Cre* (n=18) mice at 6 months post tamoxifen injection. ****-$p<0.0001$.

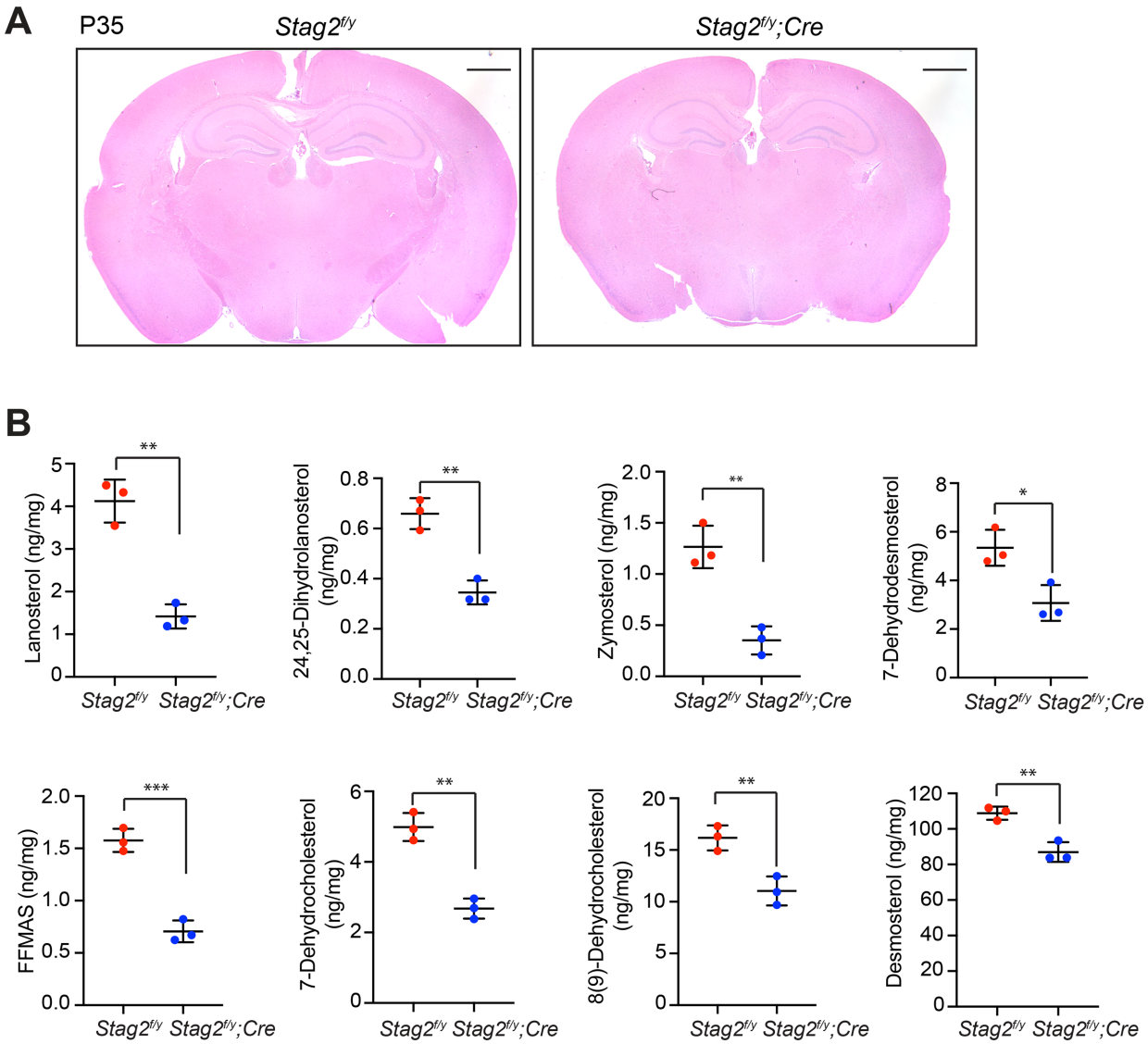

Figure S3. STAG2 deficiency in mouse brains attenuates cholesterol biosynthesis.
(A) H&E staining of the coronal sections of *Stag2$^{f/y}$* and *Stag2$^{f/y}$;Cre* mouse brains. Scale bar, 1 mm.
(B) Mass spectrometry analysis of cholesterol precursors in *Stag2$^{f/y}$* and *Stag2$^{f/y}$;Cre* brains. n = 3 mice per genotype. *p < 0.05, **p < 0.01, ***p < 0.001; Mean ± SD.

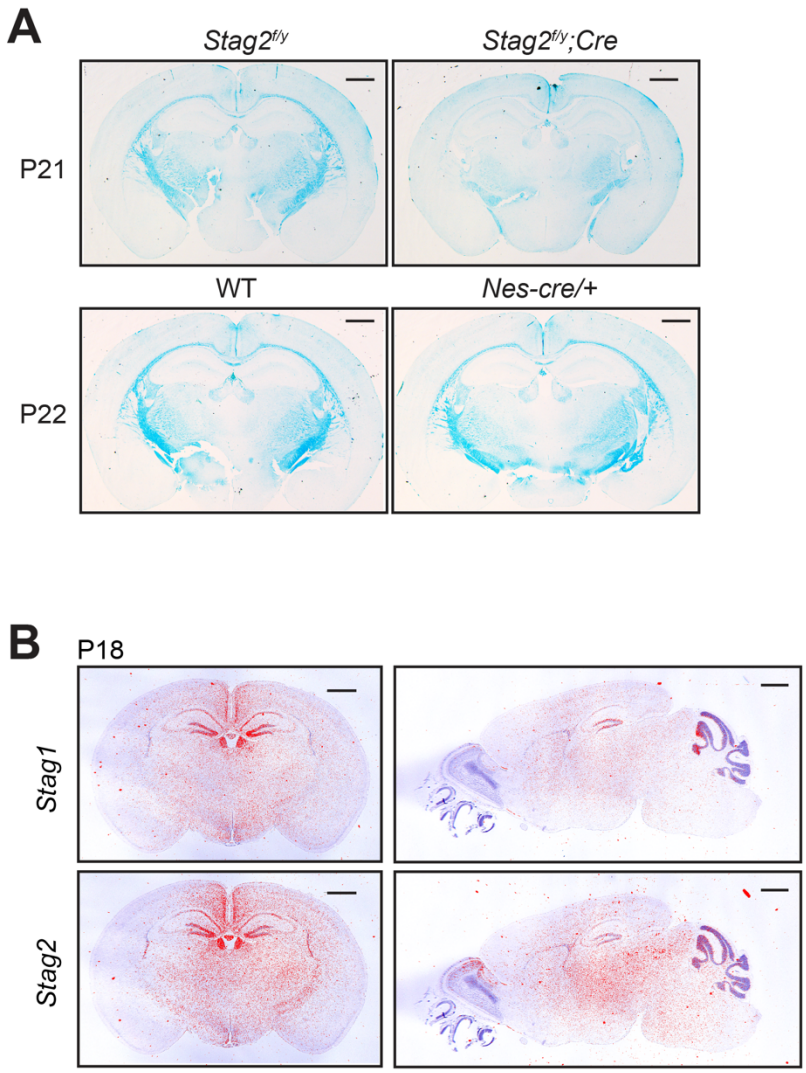

Figure S4. Brain-specific *Stag2* deletion impairs CNS myelination.
(A) Luxol fast blue staining of the coronal brain sections of mice with the indicated genotypes. n = 3 mice each for *Stag2*$^{f/y}$ and *Stag2*$^{f/y}$*;Cre* genotypes. n = 2 mice each for WT and *Nes-Cre/+* groups. animals per genotype. Scale bar = 1 mm.
(B) In situ hybridization of ^{35}S-labeled RNA probes of the coronal (left) and sagittal (right) sections of WT mouse brains. Bright field images (purple) were overlaid with autoradiography images (red). Scale bar = 1 mm.

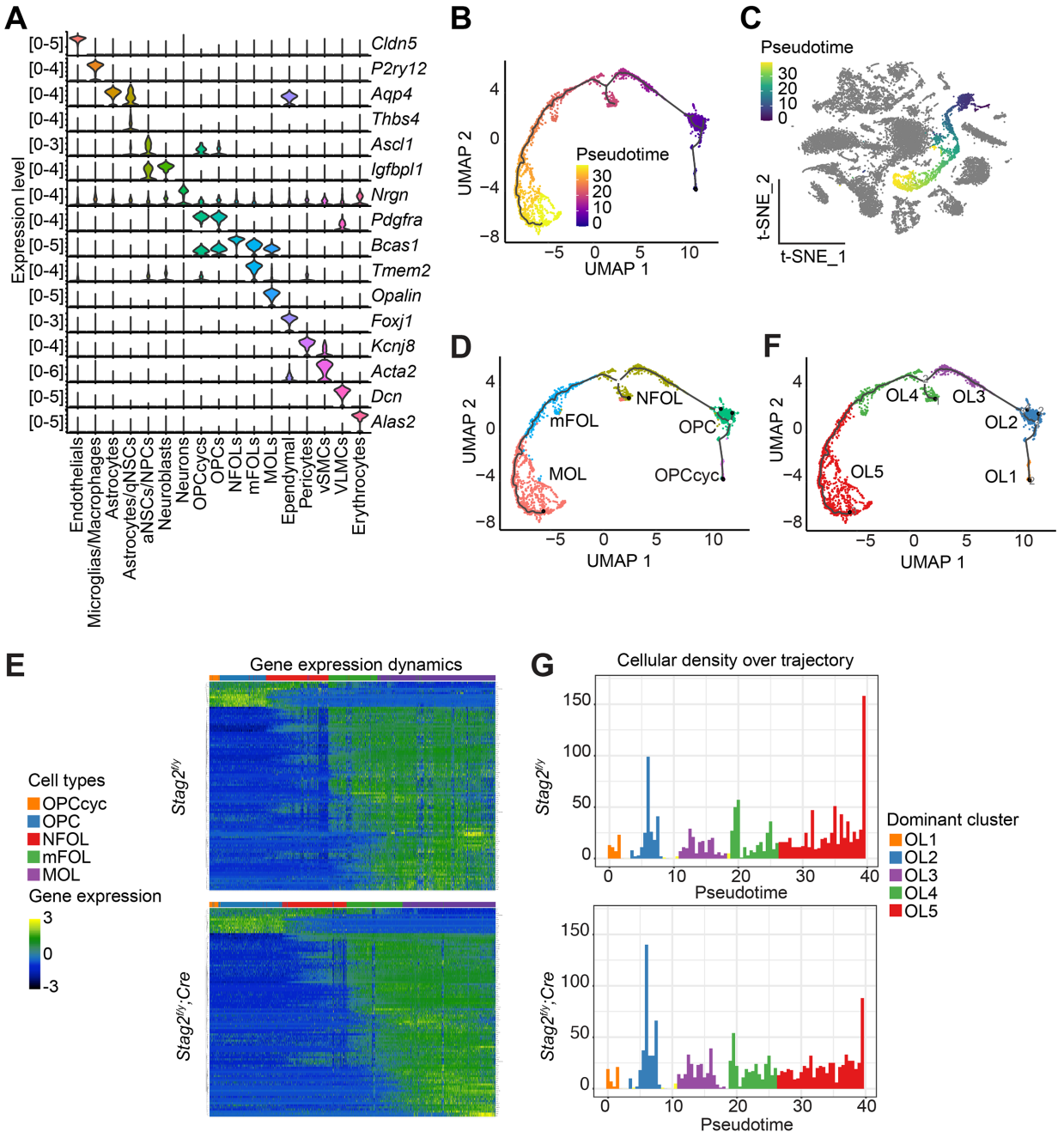

Figure S5. *Stag2* deletion causes differentiation delay in the oligodendrocyte lineage.
(A) Violin plot of the expression levels of feature genes of the indicated brain cell types.
(B) Trajectory inference analysis of oligodendrocyte (OL) lineage cells extracted from the single-cell RNA-seq dataset using Monocle3. Cells are colored from purple to yellow by pseudotime variables.
(C) OL differentiation trajectory in the *t-SNE* plot. The OL lineage is colored from navy blue to yellow by pseudotime variables. Cells of other lineages are colored grey.
(D) Distribution of the assigned OL cell types along the trajectory.

(E) Heatmap of gene expression dynamics over pseudotime along the OL differentiation trajectory. Each row represents one of the top 100 most variable genes along pseudotime. Each column represents a single cell.
(F) Re-clustered OL subgroups in the trajectory inference analysis.
(G) Cell density across pseudotime for the OL differentiation trajectory. Dominant clusters for each pseudotime bin are color labeled as in (F).

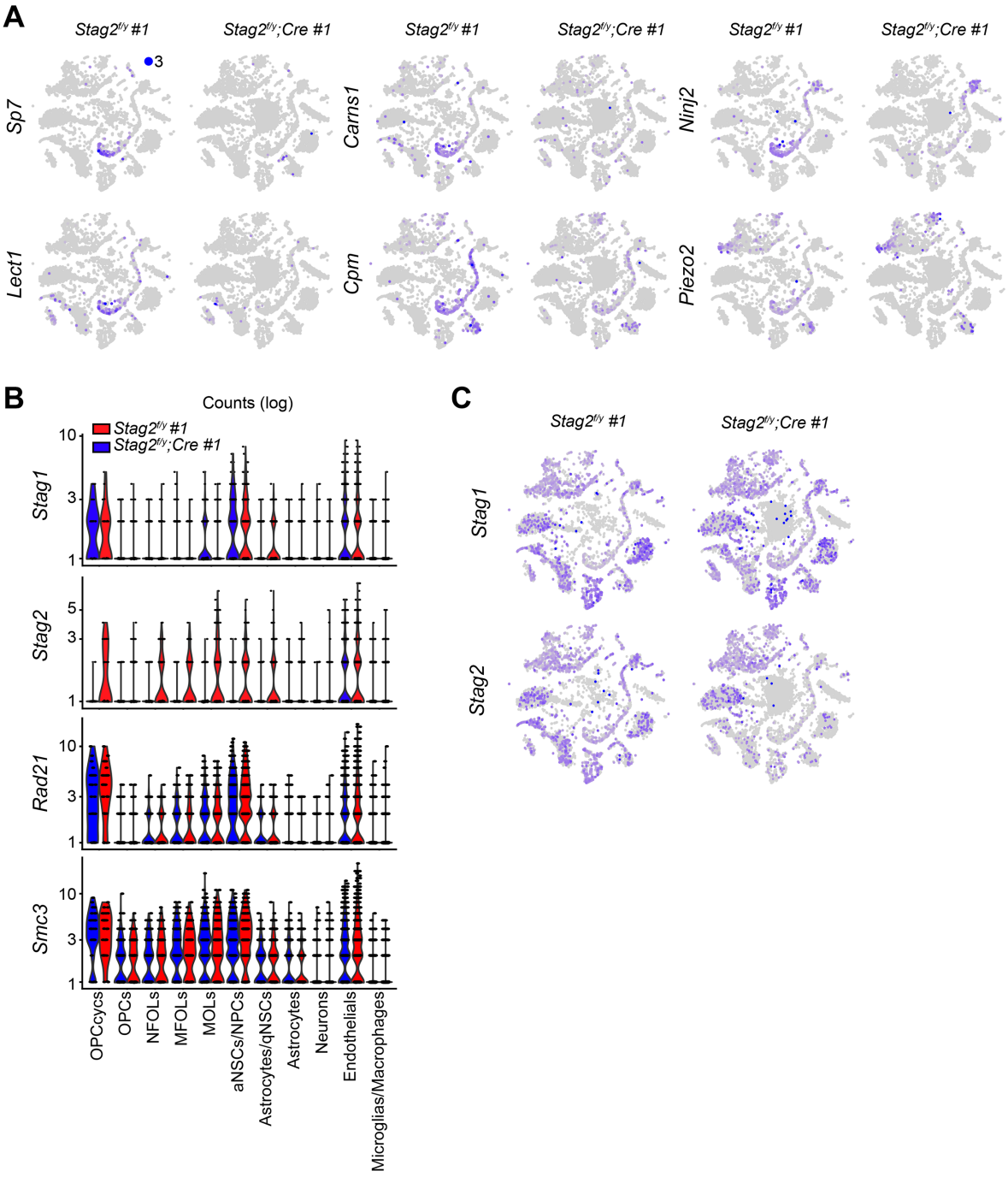

Figure S6. STAG2 regulates the transcription of oligodendrocyte genes.
(A) FeaturePlot of the expression levels of representative down-regulated genes in the *Stag2$^{f/y}$;Cre* whole brains. Maximum cutoff of 3 was used.
(B) Violin plot of the expression of cohesin subunit genes in the indicated brain cell types from the scRNA-seq transcriptome analysis.
(C) FeaturePlot of the expression of *Stag1* and *Stag2* in *Stag2$^{f/y}$* and *Stag2$^{f/y}$;Cre* forebrains. Maximum cutoff of 3 was used.

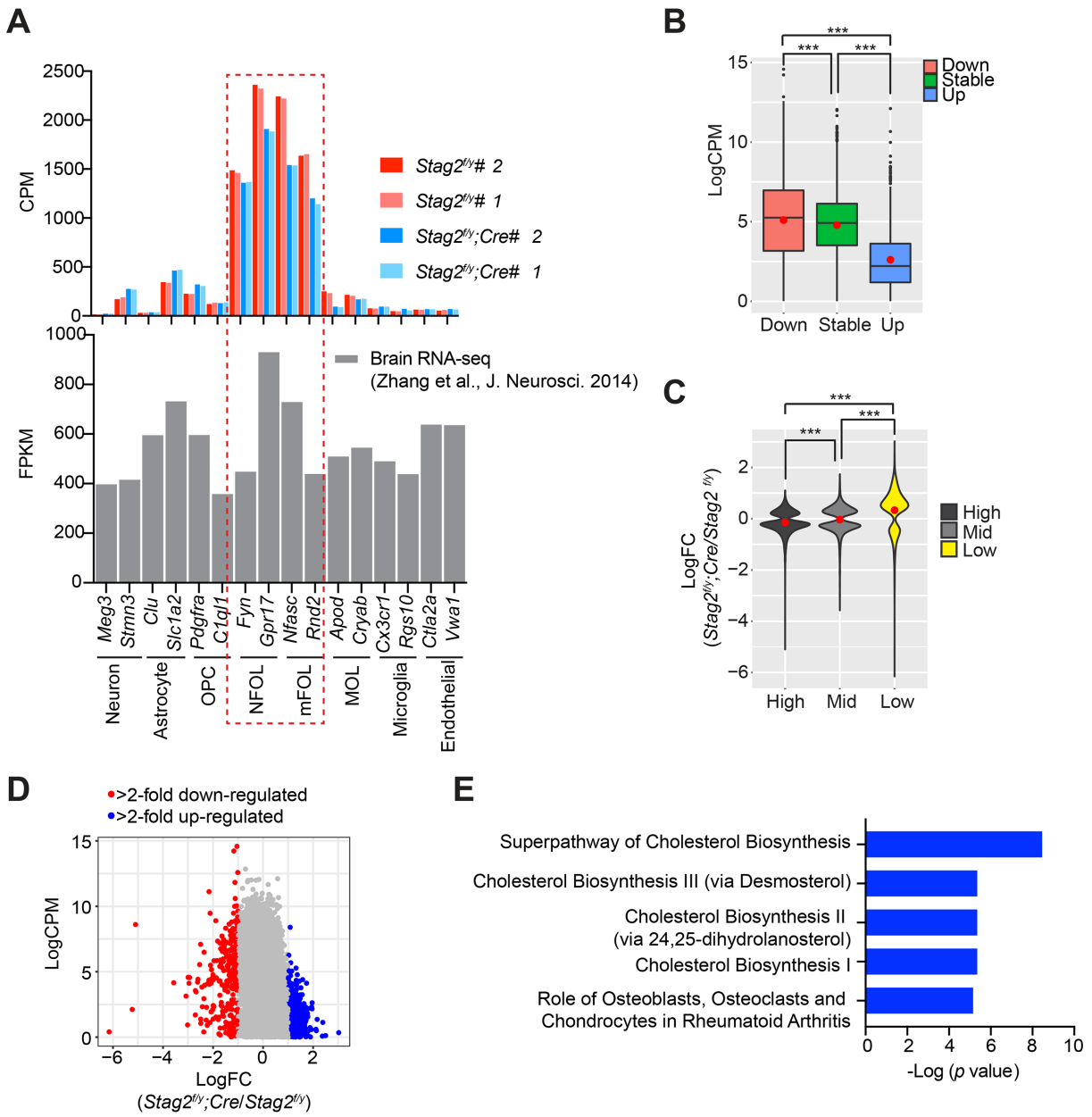

Figure S7. STAG2 regulates transcription in primary oligodendrocytes.
(A) The expression levels of signature genes of indicated brain cell types in the isolated primary oligodendrocytes (OLs) in this study. The expression levels of the same set of signature genes in the individually isolated cell types from previous studies are shown below. NFOL and mFOL signature genes are highly enriched in the isolated primary OLs in this study.
(B) Boxplot of the expression levels for genes in the indicated categories. Red dots represent the mean values. ***$p < 0.001$.
(C) Violin plot of the expression changes for the active genes with different expression levels. Red dots represent the mean value. ***$p < 0.001$.
(D) Scatter plot of the gene expression level against transcriptional changes.
(E) IPA analysis of the down-regulated gene sets.

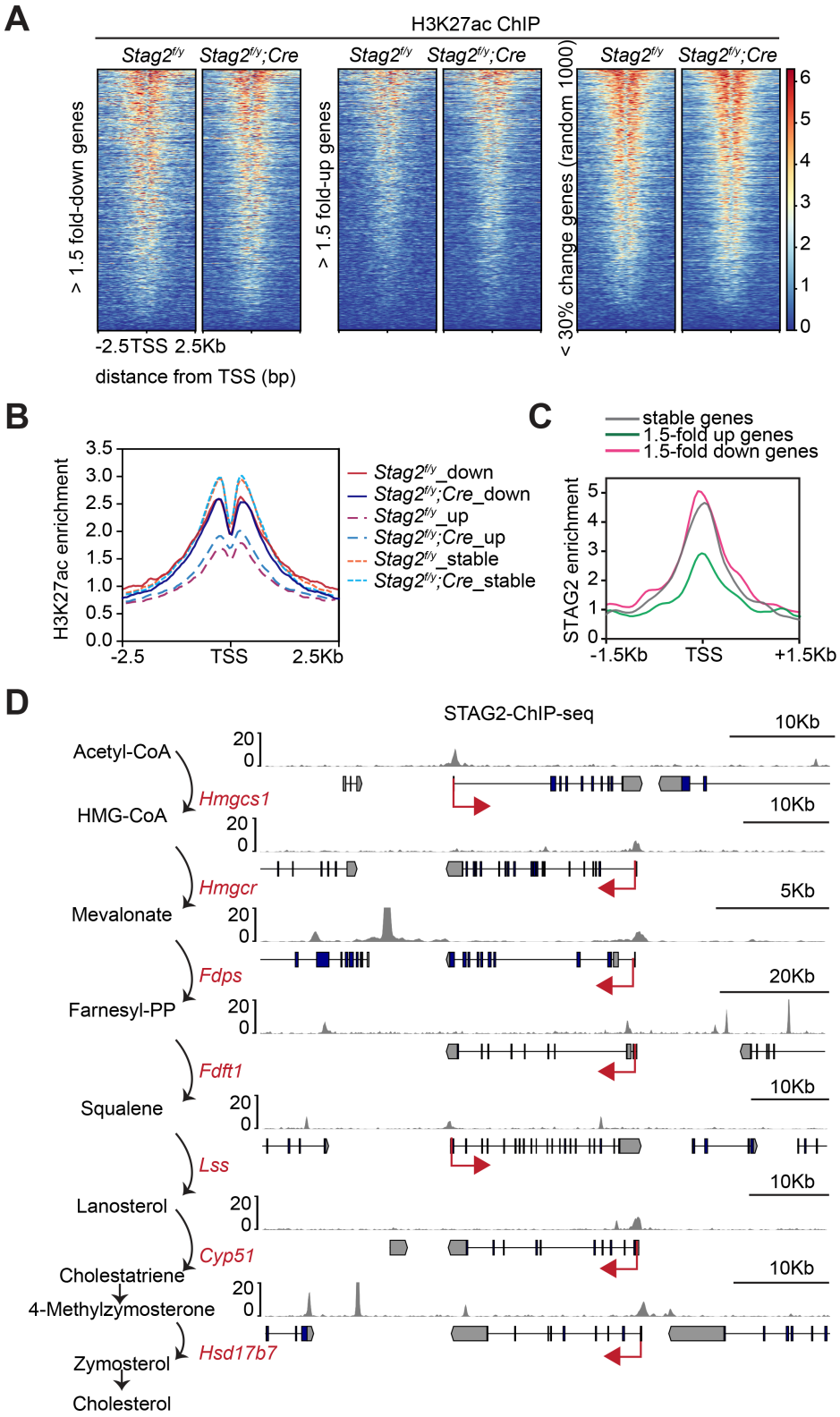

Figure S8. Enrichment of STAG2 and histone modifications at gene promoters.

(A) Heatmap of H3K27ac ChIP-seq signal enrichment in the promoter regions of genes in the indicated categories.
(B) Density profile of H3K27ac ChIP-seq signal enrichment in the promoter regions of genes in the indicated categories.
(C) Density profile of STAG2 ChIP-seq signal enrichment in the promoter regions of genes in the indicated categories.
(D) Binding of STAG2 at the genomic loci of down-regulated genes that encode cholesterol biosynthetic enzymes as revealed by ChIP-seq.

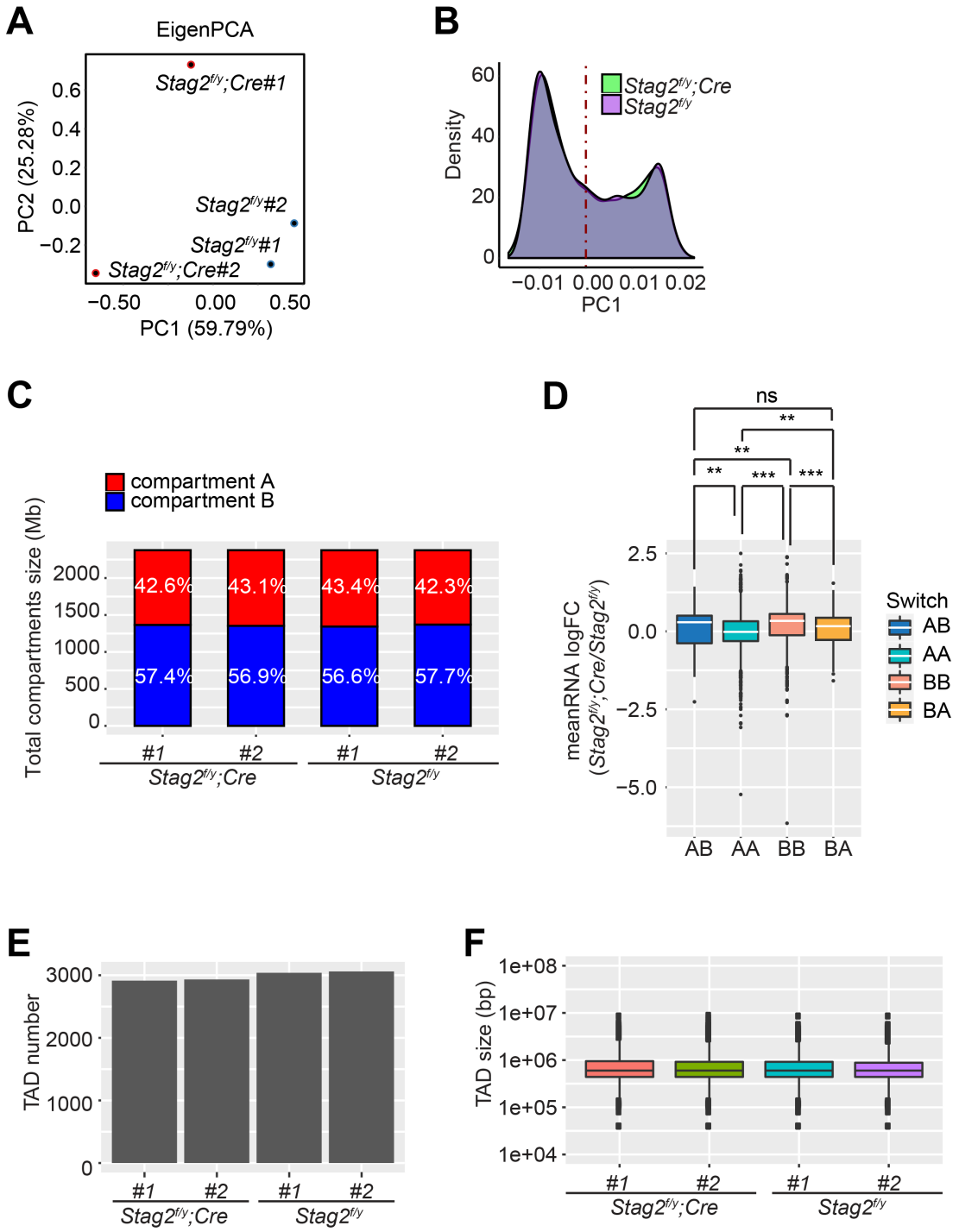

Figure S9. *Stag2* deletion does not alter chromatin compartmentalization or TAD formation in oligodendrocytes.

(A) Principal component analysis (PCA) plot of the eigenvectors of the indicated samples.

(B) Density plot of principal component 1 (PC1) of *Stag2*$^{f/y}$ and *Stag2*$^{f/y}$*;Cre* oligodendrocytes.

(C) Compartment compositions of the indicated samples.

(D) Boxplot of the average gene expression change for all the differentially expressed genes (FDR < 0.05) inside each genomic bin. Bins counted: AA, 5806; AB, 155; BA, 251; BB, 2659. The unpaired Wilcoxon-test was used for the statistical analysis. *p < 0.05; **p < 0.01; ***p < 0.001; ns, not significant.
(E) TAD numbers of the indicated samples.
(F) TAD size distributions of the indicated samples.

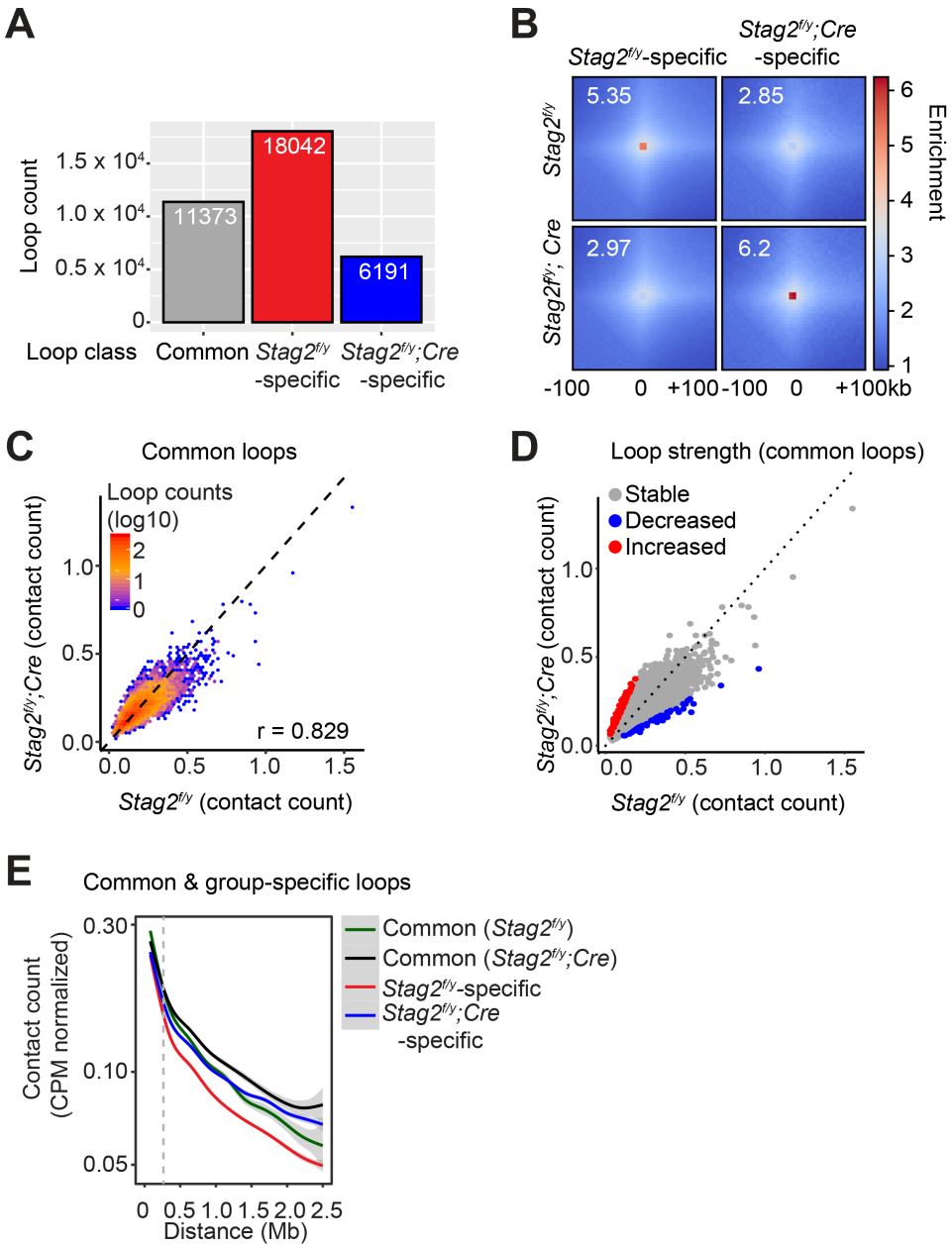

Figure S10. *Stag2* deletion reduces chromatin loops in oligodendrocytes.
(A) Loop numbers of the indicated categories.
(B) Pile-up analysis of loop "dots"-centered local contact maps for loops specific to *Stag2*$^{f/y}$ or *Stag2*$^{f/y}$*;Cre* oligodendrocytes (OLs).
(C) Hexbin plot of contact counts of common loops in *Stag2*$^{f/y}$ and *Stag2*$^{f/y}$*;Cre* OLs.
(D) Scatter plot of contact counts of common loops in *Stag2*$^{f/y}$ and *Stag2*$^{f/y}$*;Cre* OLs. Loops with significantly changed strength in *Stag2*$^{f/y}$*;Cre* OLs are highlighted in red (increased) and blue (decreased). Log_2FC threshold of 1 was used.
(E) Normalized contact counts for loops in the indicated categories across different genomic distances.

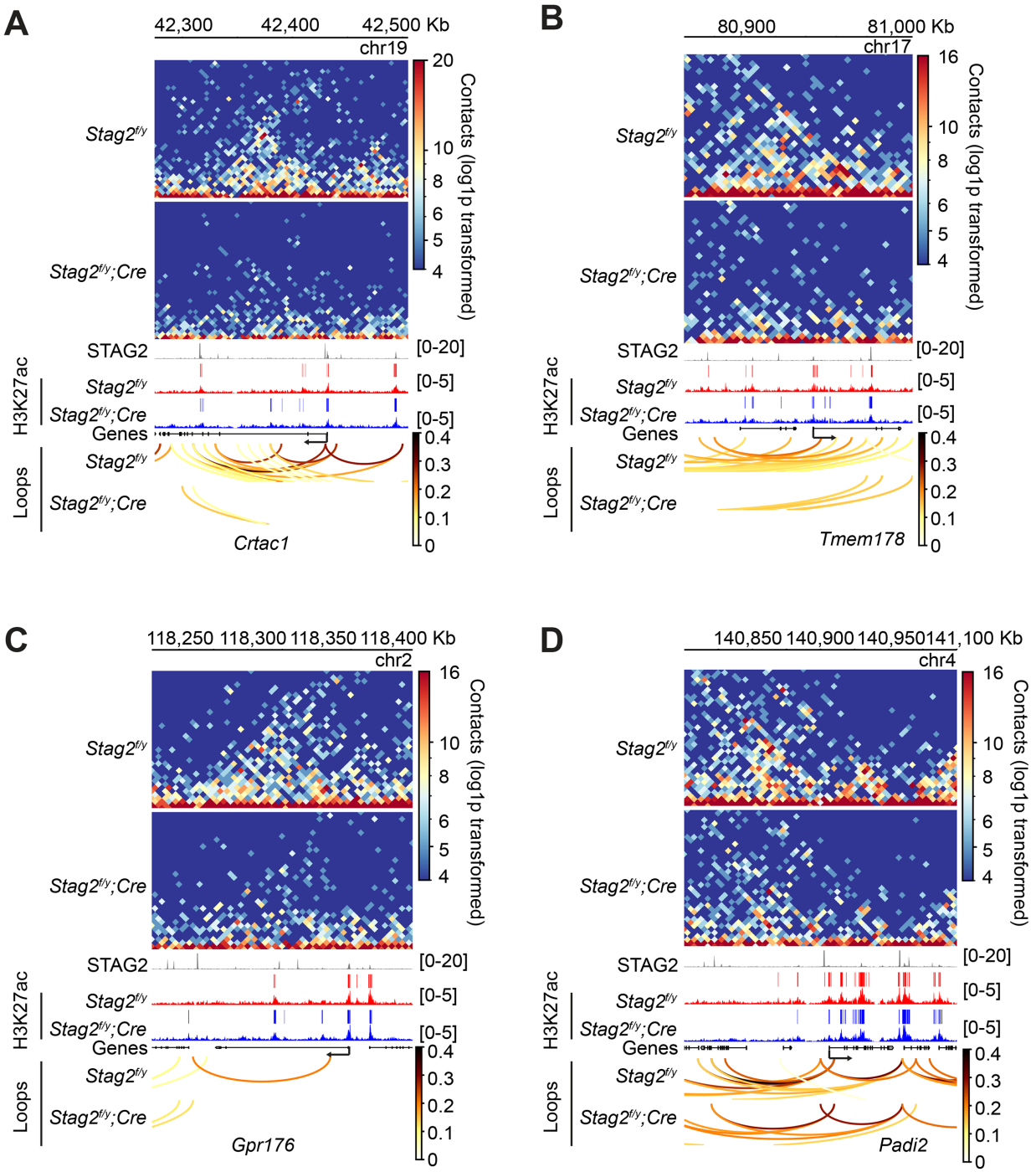

Figure S11. STAG2 controls local chromatin looping at differentially regulated genes. (A-D) Snapshots of the contact maps at the indicated differentially regulated genes. Tracks and peaks from STAG2 and H3K27ac ChIP-seq as well as loops are shown below. Transcription directions are indicated by arrows.

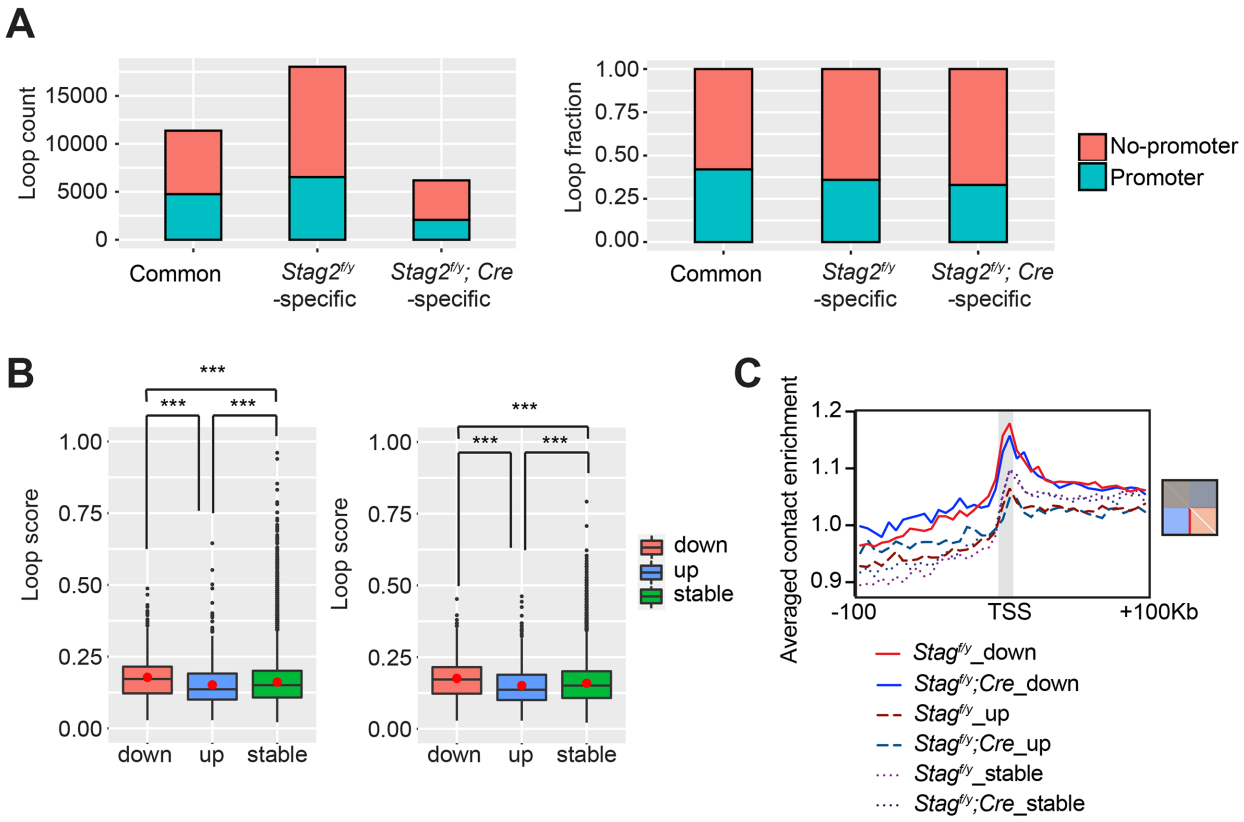

Figure S12. STAG2 regulates the formation of promoter-anchored loops in oligodendrocytes.
(A) Loop counts (left panel) and fractions (right panel) of loops anchored at promoter or non-promoter regions in the indicated categories.
(B) Loop score of the loops in Figure 6E. Loop score from *Stag2*$^{f/y}$ oligodendrocytes (OLs) was used for common loops on the left, and loop score from *Stag2*$^{f/y}$*;Cre* OLs was used for common loops on the right. The unpaired Wilcoxon test was used for the statistical analysis. ***$p < 0.001$.
(C) Profile plot of the average enrichment score for the bottom half of each graph panel in Figure 6F. Diagonal pixels were omitted.